Molecular Omics, 2026, 22(5), aaiag022
https://doi.org/10.1093/molecular-omics/aaiag022
Published: 10 September 2026
Research Article

OXFORD

Baseline cellular state shapes the molecular impact of mutant *Kirsten rat sarcoma viral oncogene homologue* (*KRAS*) alleles in reconstituted pancreatic cancer cells

Yanixa Quiñones-Avilés[1,2,3,‡], Barbora Salovska[1,4,‡], Cassandra S. Markham[1,2,3], Yi Di[1,4], Benjamin E. Turk[3,4,5], Yansheng Liu[1,3,4,5,6,*], Mandar Deepak Muzumdar[1,2,3,5,7,*]

[1]Yale Cancer Biology Institute, Yale University, West Haven, CT 06516, United States
[2]Department of Genetics, Yale University School of Medicine, New Haven, CT 06520, United States
[3]Combined Program in the Biological and Biomedical Sciences, Graduate School of Arts and Sciences, Yale University, New Haven, CT 06520, United States
[4]Department of Pharmacology, Yale University School of Medicine, New Haven, CT 06520, United States
[5]Yale Cancer Center, Yale University School of Medicine, New Haven, CT 06510, United States
[6]Department of Biomedical Informatics & Data Science, Yale University School of Medicine, New Haven, CT 06510, United States
[7]Department of Internal Medicine, Section of Medical Oncology and Hematology, Yale University School of Medicine, New Haven, CT 06510, United States
[*]Corresponding authors. Yansheng Liu, Yale Cancer Biology Institute, Yale University, West Haven, CT 06516, USA. E-mail: yansheng.liu@yale.edu; Mandar Deepak Muzumdar, Yale Cancer Biology Institute, Yale University, West Haven, CT 06516, USA. E-mail: mandar.muzumdar@yale.edu.
[‡]Authors Yanixa Quiñones-Avilés and Barbora Salovska contributed equally to this work.

Abstract

Kirsten rat sarcoma viral oncogene homologue **(*KRAS*) is mutated in over 90% of pancreatic ductal adenocarcinomas (PDAC), where hotspot alterations in codons 12, 13, and 61 drive tumour initiation and progression. Although distinct biochemical properties have been described for individual KRAS mutants, whether they generate unique allele-specific signalling programmes in PDAC cells remains unresolved. Here, we systematically interrogated the molecular consequences of seven common KRAS mutant variants in reconstituted isogenic, KRAS-deficient PDAC cell lines by integrated transcriptomic, proteomic, and phosphoproteomic profiling. We found that baseline cellular state, rather than allele identity, was the predominant driver of molecular variation. Comparisons with established KRAS reference signatures revealed significant but moderate overlap at the mRNA level and less so at the proteome level. Pathway analyses highlighted the interferon response and mitochondrial translation-related proteins as recurrently altered across mutant alleles, while phosphoproteomic data confirmed robust extracellular signal-regulated kinase 1/2 (ERK1/2) activity and the suppression of dual-specificity tyrosine phosphorylation-regulated kinase substrates by mutant KRAS expression. Importantly, no robust mutant allele-specific molecular programmes were identified in our KRAS-reconstituted cell lines. Together, our study establishes a comprehensive multi-omics resource for KRAS signalling in PDAC and demonstrates that cellular context exerts a stronger influence than allele identity in shaping molecular profiles, with implications for interpreting putative allele-specific signalling dependencies.**

Introduction

Pancreatic ductal adenocarcinoma (PDAC) is the third leading cause of cancer-related death in the USA and is predicted to become the second by 2030 [1]. *Kirsten rat sarcoma viral oncogene homologue* (*KRAS*) mutations are considered the initiating event in PDAC development, with activating *KRAS* mutations being found in over 90% of human PDAC tumours [2]. Single-point mutations in amino acids G12, G13, and Q61 disrupt KRAS inactivation by guanosine triphosphatase activating proteins (GAPs), rendering KRAS near constitutively active and facilitating tumorigenesis [3]. While these hotspot residues can harbour multiple substitutions, the most common alleles observed in PDAC are $KRAS^{G12D}$, $KRAS^{G12V}$, and $KRAS^{G12R}$, together accounting for nearly 90% of cases [2].

Mutant KRAS proteins reportedly possess unique biochemical properties, such as distinct intrinsic and GAP-stimulated guanosine triphosphate (GTP) hydrolysis rates, intrinsic and Son of Sevenless (SOS)-stimulated nucleotide exchange rates, and binding affinities to the Rat sarcoma viral oncogene (RAS)-binding domain of effector RAF kinases [4, 5], supporting the potential for divergent allele-specific signalling networks that underscore unique vulnerabilities and response to treatment. Indeed, previous studies comparing the phosphoproteomic landscape of $KRAS^{G12D}$ and $KRAS^{G13D}$ mutants in isogenic colorectal cancer cell lines have reported mutant-specific

Received: 12 June 2026. **Revised:** 10 August 2026. **Accepted:** 6 September 2026
© The Author(s) 2026. Published by Oxford University Press.
This is an Open Access article distributed under the terms of the Creative Commons Attribution-NonCommercial License (https://creativecommons.org/licenses/by-nc/4.0/), which permits non-commercial re-use, distribution, and reproduction in any medium, provided the original work is properly cited. For commercial re-use, please contact reprints@oup.com for reprints and translation rights for reprints. All other permissions can be obtained through our RightsLink service via the Permissions link on the article page on our site—for further information please contact journals.permissions@oup.com.

proteomic and phosphoproteomic signatures [6, 7]. In addition to these biochemical and signalling differences, biological distinctions among KRAS mutants have been reported. For example, unlike $KRAS^{G12D}$ and $KRAS^{G12V}$, $KRAS^{G12R}$ cannot stimulate macropinocytosis due to its impaired ability to engage the catalytic p110α subunit of phosphoinositide 3-kinase (PI3K), suggesting allele-specific biology [8]. Consistent with these observations, a comparison of common and uncommon KRAS mutants in isogenic MCF10A mammary epithelial cells showed that distinct alleles had differential effects on epidermal growth factor (EGF)-independent proliferation and anchorage-independent growth [9]. While these studies highlight important KRAS mutant-specific biochemical and biological differences, they have largely focused on discrete comparisons of a small subset of alleles in non-pancreatic or non-malignant systems, underscoring the need to comprehensively interrogate the molecular programmes engaged by a broader panel of *KRAS* mutations in relevant PDAC models.

To explore the molecular impact of different *KRAS* alleles, we generated a panel of four KRAS-deficient human PDAC cell lines using clustered regularly interspaced short palindromic repeats (CRISPR)/Cas9-mediated gene editing and established isogenic cells reconstituted to express wild-type (WT) or seven common mutant KRAS variants. We combined RNA-sequencing (RNA-Seq) and data-independent acquisition mass spectrometry (DIA-MS) to profile transcriptomic, proteomic, and phosphoproteomic changes driven by KRAS variants under steady-state conditions. Interestingly, we found that baseline cellular state, rather than the specific mutation, largely shaped the global impact of KRAS variants in our panel of reconstituted PDAC cell lines. Convergent transcriptomic and proteomic pan-mutant KRAS signatures revealed alterations in the expression of interferon response pathway genes and mitochondrial translation-related proteins and the abundance of extracellular signal-regulated kinase 1/2 (ERK1/2) and dual-specificity tyrosine phosphorylation-regulated kinase (DYRK) substrate phosphosites, which partially overlapped with recently reported KRAS mutant signatures derived from other cell lines or cancer types [10–12]. Taken together, our study establishes a comprehensive multi-omics resource for defining and comparing KRAS mutant signatures in PDAC. Further, our findings suggest that baseline cellular states and signalling context exert a stronger influence than allele identity, with important implications for interpreting putative allele-specific signalling in PDAC and potentially other *KRAS* mutant cancers.

Methods

Cell lines and cell culture conditions

Established human PDAC 8988T (ACC162) and KP4 (RCB1005) cell lines were obtained from the Leibniz Institute DSMZ-German Collection of Microorganisms and Cell Cultures GmbH and RIKEN, respectively. 293FS∗ cells used for lentivirus production were a gift from Dr N. Joshi. RAS-less mouse embryonic fibroblasts reconstituted with RAS and BRAF variants were acquired from the National Cancer Institute (NCI) RAS initiative. All cell lines were confirmed negative for mycoplasma using polymerase chain reaction (PCR) testing by the Yale Molecular and Serological Diagnostics Core. Cell lines were maintained in Dulbecco's Modified Eagle Medium (DMEM) (Corning, 10-013-CV) supplemented with 10% foetal bovine serum (Thermo Fisher Scientific, A5670701) and 1% penicillin/streptomycin (Thermo Fisher Scientific, 15140122).

KRAS knockout clone generation

A single-guide RNA (sgRNA) targeting KRAS exon 2 (sequence: 5′-AATTACTACTTGCTTCCTGT-3′) was cloned into the CRISPR-Cas9 expression vector pSpCas9(BB)-2A-GFP (PX458, Addgene plasmid #48138). 1×10^6 8988T and KP4 cells were nucleofected (Amaxa) with the sgKRAS-Cas9-2A-GFP construct. Forty-eight hours later, green fluorescent protein (GFP)-positive cells were isolated by flow cytometry using a BD FACSymphony™ S6 Cell Sorter (BD Biosciences) to enrich for vector-expressing populations. After 7 days, GFP-negative cells were single-cell sorted to generate stable 8988T and KP4 clones, yielding ∼680 single-cell isolates for each parental cell line. Approximately 70 KP4 clones and 1 008 988 T clones were initially screened for KRAS expression by immunoblotting. Of the four KP4 and 408 988 T clones clearly lacking detectable KRAS protein, all KP4 clones and 138 988 T clones were further validated by PCR amplification of KRAS exon 2, as previously described [13], and amplicon next-generation sequencing using the Massachusetts General Hospital CCIB DNA Core. Three of 4 candidate KP4 clones and 12 of 13 candidate 8988T clones were confirmed as *KRAS* knockouts (KO), each harbouring out-of-frame indels at the sgRNA target site. From these, KO22 and KO63 (KP4) and KO275 and KO328 (8988T) were selected for downstream experiments.

Genomic DNA isolation and sequencing

Genomic DNA was extracted from *KRAS* KO clones and the parental cell line using the High Pure PCR Template Preparation Kit (Roche, #1179682800111). Whole-exome sequencing libraries were prepared by the Yale Center for Genome Analysis (YCGA) using the Integrated DNA Technologies (IDT) xGen V2 Exome Enrichment Kit and sequenced on the Illumina HiSeq platform (paired-end, 100-bp reads) to a mean target coverage of ∼30×.

Generation of isogenic KRAS variant-expressing pancreatic ductal adenocarcinoma cell lines

To make KRAS expression constructs (LV-PGK-eGFP-2A-KRAS), the lentiviral backbone vector (LV 1–5, Addgene #68411) was linearized by restriction enzyme digestion at designated sites. The phosphoglycerate kinase (PGK) promoter and GFP cassette were PCR-amplified from the MSCV-Puro-pGK:GFP construct (Addgene #68486) and inserted into the linearized lentiviral backbone using Gibson Assembly [New England Biolabs (NEB), #E2611] as previously described [14]. KRAS mutant cDNA sequences were PCR-amplified from the RAS Mutant Clone Collection (Addgene, Kit #1000000089) with Q5 Hot Start High-Fidelity DNA Polymerase (NEB, M0494S) using forward primers containing a NheI-HF (NEB, R3131S) or BamHI-HF (NEB, R3136S) restriction digest site and a P2A self-cleaving peptide and the reverse primer containing an AscI (NEB, R0558S) restriction digest site. PCR products were gel-purified (Qiagen, #28706), digested with respective restriction enzymes, PCR purified (Qiagen,), and ligated with the digested backbone for 1–2 h using T4 ligase (NEB, M0202S). The $KRAS^{Q61H}$ insert was generated *via* overlapping PCR to introduce the desired point mutation, followed by restriction digestion and cloning into the lentiviral backbone using the same restriction enzyme and ligation strategy described for the other *KRAS* variants. The ligation products were transformed into Stbl3 competent *Escherichia coli* (Invitrogen, C737303) and selected on ampicillin-containing agar plates. Individual positive clones were cultured

overnight in Luria-Bertani (LB) broth (Thermo Fisher Scientific, #12780052). Plasmids were purified using a QIAprep Miniprep Kit (Qiagen, #27106) and validated by Sanger sequencing performed by the W. M. Keck Biotechnology Resource Laboratory at Yale. To produce lentivirus, the lentiviral backbone, packaging vector (psPAX2, Addgene #12260), and envelope vector (VSV-G, Addgene #8454) were co-transfected into 293FS∗ cells using TransIT-LT1 (Mirus Bio, MIR2306). Culture media was changed 16 h post-transfection. Supernatants were collected at 48- and 72-h post-transfection, filtered through 0.45 μm syringe filters, and used immediately or store at −80°C prior to use. For stable KRAS expression, KRAS-deficient clones were seeded ≥16 h prior to transduction and treated with lentiviral supernatant (LV-PGK-eGFP-2A-KRAS) supplemented with 8 μg/ml polybrene (EMD Millipore, TR-1003-G). KRAS-reconstituted cells were sorted based on fluorophore intensity using a FACSymphony™ S6 Cell Sorter, wherein GFP fluorescent intensity was used as a proxy for desired KRAS expression. Cells were replated after sorting and stable fluorescence was confirmed 7 days post sort. Expression of KRAS protein was confirmed by immunoblotting.

Immunoblotting

7.5×10^5 cells were seeded per well in 6-well plates the day prior to the collection of whole cell protein lysates. For collection, cells were rinsed with cold 1× phosphate-buffered saline (PBS), scraped, pelleted, and resuspended in protein lysis buffer consisting of Pierce® Radioimmunoprecipitation Assay (RIPA) buffer (Thermo Fisher Scientific, #89900) supplemented with 1:100 0.5 M ethylenediaminetetraacetic acid (EDTA) (Thermo Fisher Scientific) and 1:100 Halt™ protease/phosphatase inhibitor cocktails (Thermo Fisher Scientific #78444), and incubated for 15 min at 4°C in a rotator. Cells were then pelleted at maximum speed (~14 000 × g) for 15 min at 4°C, and the supernatant containing the protein lysate was collected and transferred to a new microcentrifuge tube. Protein concentrations were quantified using the Pierce® Bicinchoninic Acid (BCA) Protein Assay Kit (Thermo Fisher Scientific, #23225) following the manufacturer's instructions. Equal amounts of protein (40 μg) were mixed 1:1 (by volume) with 2× Laemmli Sample Buffer (Bio-Rad, 1 610 737) containing 5% β-mercaptoethanol (Thermo Fisher Scientific, #21985023), boiled at 95°C for 5 min, loaded onto Mini-PROTEAN® 4%–20% TGX™ stain-free precast gels (Bio-Rad), and separated by Sodium Dodecyl Sulfate-Polyacrylamide Gel Electrophoresis (SDS-PAGE). Proteins were transferred onto nitrocellulose membranes using the Trans-Blot® Turbo™ Transfer System (Bio-Rad). Membranes were blocked for 1 h at room temperature in Intercept® (PBS) Blocking Buffer (LI-COR, 927-70-001) diluted 1:1 in PBS or 5% Omniblok non-fat dry milk powder (AmericanBio, AB10109-01000) in tris-buffered saline (TBS). Membranes were then incubated overnight at 4°C with primary antibodies diluted in either intercept blocking buffer with 0.1% Tween-20 (PBS-T, 1:1) or in TBS-T with 5% non-fat dry milk powder. The following antibodies were used for immunoblotting: rabbit anti-HSP90 [Cell Signalling Technologies (CST), #4877, 1:10 000], rabbit anti-pERK1/2 (T202/Y204) (CST, #4370, 1:2000), mouse anti-ERK1/2 (CST, #9107, 1:1000), rabbit anti-pAKT (S473) (CST, #4060, 1:1000), mouse anti-AKT (CST, #2966, 1:2000), and mouse anti-KRAS (Sigma-Aldrich, 3B10-2F2, 1:1000). Primary rabbit antibodies were detected with antirabbit IgG (H + L) (DyLight™ 800 4× Polyethylene Glycol (PEG) Conjugate) (CST, #5151, 1:10 000). Primary mouse antibodies were detected with antimouse IgG (H + L) (DyLight™ 680) (CST, #5470, 1:10 000) or antimouse IgGκ light chain-horseradish peroxidase (Santa Cruz Biotechnology, sc-516 102; 1:1000). Chemiluminescent detection was performed using the SuperSignal™ West Dura Extended Duration Substrate (Thermo Fisher Scientific, 34076X4). Fluorescence or chemiluminescence images were acquired under non-saturating exposure conditions using the ChemiDoc imaging system (Bio-Rad). Precision Plus Protein Kaleidoscope Prestained Protein Standards (Bio-Rad, #1610375) were used as protein size markers for individual blots. The resulting images were saved in Image Lab software (v6.1.0; Bio-Rad) format for subsequent densitometric quantification.

RNA isolation and sequencing

7.5×10^5 cells were seeded per well in six-well plates the day prior to collection. RNA was extracted using the Qiagen RNeasy Mini kit (Qiagen, #74106) following the manufacturer's protocol with RNase-free DNAse I treatment (Qiagen, #79254) to remove any genomic DNA contamination. Only high-quality RNA samples (RIN > 7), confirmed using an Agilent Bioanalyzer, were used in RNA-seq analyses. Bulk RNA-seq libraries were prepared *via* polyA selection (Illumina) and sequenced (>25 M 100-bp paired-end (2x100) reads on NovaSeq (Illumina) through the YCGA.

Protein extraction and digestion for mass spectrometry

For proteomics and phosphoproteomics analyses, a 10 M urea proteomics/phosphoproteomics lysis buffer was prepared by dissolving 10 M Urea (Thermo Fisher Scientific, #29700), 100 mM ammonium bicarbonate BioUltra (Sigma Aldrich, #1066-33-7), and Complete™ Protease Inhibitor Cocktail (Sigma-Aldrich, 11 873 580 001) in HPLC-grade water (Fisher Chemical, #7732-18-5) and was stored at −80°C. Approximately 4×10^6 cells were plated in triplicate in 10-cm dishes the day prior to protein lysate collection. Cells were rinsed twice with cold 1× PBS, scraped, and the pellets were reconstituted in 250 μl of 10 M urea proteomics/phosphoproteomics lysis buffer containing freshly added 1:100 Halt Phosphatase Inhibitor Cocktail (Thermo Fisher Scientific, #78420). Cell lysates were sonicated twice for 1 min at 4°C using a VialTweeter device (Hielscher-Ultrasound Technology). The lysates were then centrifuged at 20 000 × g for 1 h to pellet insoluble material. Supernatant containing the protein lysate was collected and transferred to a 2 ml microcentrifuge tube. Protein concentration was quantified with the Bio-Rad protein assay. Proteins were reduced with 10 mM dithiothreitol (DTT) at 56°C for 1 h, followed by alkylation with 20 mM iodoacetamide in the dark at room temperature for 1 h. The reduced and alkylated proteins were then digested using a precipitation-based protocol, as previously described [15]. Briefly, proteins were mixed with five volumes of cold precipitation solution (50% acetone, 50% ethanol, and 0.1% acetic acid) and incubated at −20°C overnight. Precipitated proteins were pelleted by centrifugation at 20 000 × g for 40 min, washed with precipitation solution, and centrifuged again under the same conditions. After removing the precipitation solution, residual solvent was evaporated in a SpeedVac (Thermo Fisher Scientific). Proteins were then digested overnight at 37°C with sequencing-grade porcine trypsin (Promega, V5111; 1:50 enzyme-to-substrate ratio) in 300 μl of 100 mM ammonium bicarbonate. The peptide mixture was desalted on C18 MacroSpin columns (NEST Group, Inc.) following the manufacturer's protocol and quantified using a NanoDrop spectrophotometer (Thermo Fisher Scientific). Two dish replicates were processed for each condition

resulting in 80 samples for the total proteome and phosphoproteome analysis.

Phosphopeptide enrichment

Phosphopeptides were enriched using the High-Select™ Fe-NTA kit (Thermo Fisher Scientific, A32992) following the manufacturer's protocol [16]. Briefly, the peptide–resin suspension was incubated for 30 min at room temperature with gentle shaking every 10 min, then transferred to a filter tip (TF-20-L-R-S, Axygen) and centrifuged to discard the flow-through. The resin was then washed three times with 200 μl of wash buffer (80% acetonitrile and 0.1% trifluoroacetic acid) and twice with 200 μl of H_2O. Phosphopeptides were eluted twice with 100 μl of elution buffer (50% acetonitrile and 50% $NH_3 \cdot H_2O$), dried in a SpeedVac, and quantified by NanoDrop.

Mass spectrometry measurements

For liquid chromatography–mass spectrometry (LC–MS) analysis, peptides were analysed as described previously [15, 17]. Peptide separation was carried out using an EASY-nLC 1 200 system (Thermo Fisher Scientific) with a self-packed PicoFrit column (New Objective; 75 μm × 50 cm) containing ReproSil-Pur 120A C18-Q 1.9 μm resin (Dr Maisch GmbH, Ammerbuch, Germany). Peptides were eluted over a 150-min gradient from 4% to 37% buffer B (80% acetonitrile and 0.1% formic acid) with buffer A (0.1% formic acid in water) at a flow rate of 300 nl/min, while maintaining the column at 60°C (PRSO-V1 oven, Sonation GmbH). Eluted peptides were analysed on an Orbitrap Fusion Lumos Tribrid mass spectrometer (Thermo Fisher Scientific) equipped with a NanoFlex ion source (spray voltage 2000 V, capillary temperature 275°C). The data independent acquisition mass spectrometry (DIA-MS) acquisition consisted of an MS1 survey scan followed by 33 variable-window MS2 scans, as described previously [18, 19]. MS1 scans were acquired from 350 to 1650 *m*/*z* at a resolution of 120 000 (*m*/*z* 200) with an Automated Gain Control (AGC) target of 2.0E6 and a maximum injection time of 50 ms. MS2 scans were collected at a resolution of 30 000 (*m*/*z* 200) using High-energy Collisonal Dissociation (HCD) with 28% normalized collision energy, an AGC target of 1.5E6, and a maximum injection time of 52 ms. The default precursor charge state was set to 2, and both MS1 and MS2 spectra were recorded in profile mode.

Quantification and statistical analysis

Immunoblot quantification and statistical analysis

Protein quantification from immunoblots was performed using Image Lab software (v6.1.0; Bio-Rad). Bands corresponding to the protein of interest were defined using the Lane and Band detection tools, and background subtraction was applied using the local background method. Integrated adjusted band intensities were initially normalized to the corresponding loading control (HSP90). Phosphorylated AKT (pAKT) and ERK1/2 (pERK1/2) were then normalized to their non-phosphorylated counterparts AKT and ERK1/2, respectively. All samples were then normalized to $KRAS^{WT.}$ Normalized ratios from $n = 3$ biological replicates are presented as mean ± SEM or geometric mean ± geometric SD in bar graphs and then analysed using one-way repeated measures analysis of variance (ANOVA) with Tukey's or Dunnett's *post hoc* test or Brown-Forsythe lognormal ANOVA with Games-Howell's *post hoc* test in Prism v10.6.0 (Graphpad Software). $P < .05$ was used as level of significance for all statistical analyses.

Whole exome sequencing analysis and variant detection

Raw whole exome sequencing data were processed on the Galaxy web platform to generate analysis-ready BAM files. Preprocessing steps included read filtering using Filter BAM datasets on a variety of attributes (Galaxy v2.4.1), duplicate removal using RmDup (Galaxy v2.0.1), indel left-alignment using BamLeftAlign (Galaxy v1.3.1), and recalculation of MD tags and mapping qualities using CalMD (Galaxy v2.0.2). The resulting CalMD-corrected BAM files from each CRISPR-edited clone were paired with the corresponding parental cell line BAMs, which served as matched normal controls, for somatic variant calling against the hg19 reference genome.

Somatic variant detection was performed using the Galaxy Somatic Variant Calling workflow incorporating VarScan Somatic (Galaxy tool v2.4.3.6). VarScan was executed with customized variant-calling parameters, including a minimum base quality of 28 and a minimum mapping quality of 1, while all other calling and posterior filtering parameters were retained at their default settings. Normal sample purity and tumour sample purity were both explicitly specified as 1.0, reflecting the clonal nature of the cell line samples. Under VarScan's somatic classification criteria, variants were considered somatic if the tumour variant allele frequency (VAF) was ≥10%, the normal VAF was ≤2%, minimum depth and supporting read thresholds were met, and the somatic *P*-value was ≤.05. Identified single-nucleotide variants (SNVs) and indels were functionally annotated using SnpEff (Galaxy v4.3 + T.galaxy1) and further annotated with information from ClinVar, dbSNP, the COSMIC Cancer Gene Census (CGC), and the Cancer Genome Interpreter (CGI). Coding variants were summarized in a protein-effect table reporting allele frequencies, predicted amino-acid substitutions, and cancer-associated gene annotations. The Galaxy workflow was adapted from the Galaxy Training Network tutorial 'Identification of somatic and germline variants from tumour and normal sample pairs' (https://training.galaxyproject.org/training-material/topics/variant-analysis/tutorials/somatic-variants/tutorial.html).

Copy-number variation (CNV) analysis was performed in R (v4.3.2) using the Bioconductor package cn.mops (v1.48.0), with supporting packages GenomicRanges (v1.54.1) and GenomicFeatures (v1.54.4). Read depth was quantified across hybrid-capture target regions extended by ±30 bp, and an exome-optimized model was used to infer copy-number gains and losses. CNV segments were overlapped with gene coordinates from the UCSC hg19 reference annotation, and affected genes were cross-referenced with curated cancer gene resources including COSMIC CGC, ClinVar, and CGI.

RNA-sequencing analysis

Low-quality bases and adapter sequences were trimmed using Trim Galore (v0.6.10). Cleaned reads were aligned to the Gencode human genome (Release 48; version GRCh38.p14) using the STAR aligner (v2.7.7a). Differential gene expression analysis was performed using DESeq2 (v1.46.0) [20]. Data were prefiltered to remove low-expressing genes (≤10). Genes with a fold change of ≥1.3 and an adjusted *P*-value ≤ .05 were considered differentially expressed. Three comparisons were performed separately for each clone: (i) each KRAS mutant ($n = 1$) was tested against two KRAS WT ($KRAS^{WT}$) controls ($n = 2$) to find mutant-specific signatures, (ii) all samples from the KRAS mutant conditions ($n = 7$) were tested against KRAS WT controls ($n = 2$) to find pan-mutant signatures, and (iii) all samples from the 'DVR' subtype (comprising $KRAS^{G12D}$, $KRAS^{G12V}$, and $KRAS^{G12R}$; $n = 3$) and 'Other'

subtype ($KRAS^{G12C}$, $KRAS^{G13C}$, $KRAS^{Q61H}$, $KRAS^{Q61R}$; $n = 4$) were tested against $KRAS^{WT}$ controls ($n = 2$) to find DVR signatures. All RNA-seq analyses were conducted in R (v4.4.2).

Mass spectrometry data processing

Label-free data were analysed in Spectronaut v19 using the directDIA+ [19] workflow against the human SwissProt database supplemented with manually added KRAS mutant sequences (20 426 entries, downloaded March 2025), applying default Spectronaut settings [21]. For total proteome searches, carbamidomethylation of cysteine was set as a fixed modification, while methionine oxidation and N-terminal acetylation were specified as variable modifications. In phosphoproteome searches, phosphorylation of serine, threonine, and tyrosine (S/T/Y) was additionally included as a variable modification. Peptide- and protein-level false discovery rates (FDRs) were controlled at 1%, and data were filtered by Qvalue. Post-translational modification (PTM) site localization in Spectronaut v14 was performed using the PTM function with a score cutoff of >0.75 [22, 23]. All other Spectronaut parameters were left at default, with 'Interference Correction' enabled and 'Global Normalization (Median)' applied. The precursor and experiment-wide protein *Q*-values were set to 0.01, while the run-wise protein *Q*-value was 0.05. Protein and peptide quantification were based on the top 3 precursors and top 3 stripped peptide sequences, respectively. Total proteome data were exported *via* the protein pivot report, using PG.ProteinGroups as the unique identifier and PG.Quantity for quantification. Phosphoproteome data were exported *via* the peptide pivot report, with EG.PrecursorId as the unique identifier and EG.TotalQuantity as the quantification column. Relative intensities below 10 were replaced with NA, followed by $\log_2$ transformation and normalization using the limma::normalize.cyclic.loess() function [24]. For phosphoproteome analysis, precursor-level pivot reports were exported from Spectronaut using two PTM localization score cutoffs (0.75 and 0), following the strategy outlined in our previous work [21]. Briefly, the first report (localization probability >0.75; class I sites [25]; $n = 116\,086$ unique modified precursors) was used to identify confidently localized phosphopeptides. The second report (localization probability >0; $n = 181\,427$ unique precursors) was restricted to the precursors from the first report and served to extract intensity values. To define representative phosphopeptides (phos.id), we selected: (i) the precursor with the greatest number of valid values across the 80 MS runs, and (ii) if tied, the precursor with the highest summed intensity. This yielded 63 448 unique phos.ids from 5967 phosphoprotein groups, preserving information on multiply phosphorylated peptides for downstream analyses. These mapped to 56 768 unique phosphorylation sites. Phosphoprecursor intensities below eight were excluded, and the data were $\log_2$ transformed and normalized using the limma::normalize.cyclic.loess() function [24]. Two samples with low quality (number of quantified unique phos.ids below 20 000; both replicates of K22 $KRAS^{G13C}$) were repeated in another batch replicate, leading to an improved and comparable coverage (~37 000 IDs). However, even after a batch effect removal attempt using harmonizR [26], the repeated sample showed a notable experimental batch effect and thus was rigorously reported but excluded from downstream analysis. Sequence windows flanking the modification site (15-mers) were extracted using the PTMoreR package (1.1.0) [27]. To confirm comparable KRAS expression across variants using our DIA-MS data, we extracted precursor intensities for KRAS peptides and filtered them to exclude sequences mapping to neuroblastoma rat sarcoma viral oncogene homologue (NRAS) or Harvey rat sarcoma viral oncogene homologue (HRAS). Seven unique KRAS-specific peptide precursors were identified and a representative peptide consistently detected across all samples was used to confirm comparable KRAS abundance across variants.

Statistical analysis of proteomics data

Statistical analysis was performed in R using the limma package (3.58.1) [28] with the standard workflow (lmFit(), contrasts.fit(), eBayes()). Multiple testing correction was applied using the Benjamini–Hochberg FDR method, with significance defined as FDR < 0.05 and absolute fold change > 1.3. Moderated $\log_2$ fold changes from limma were used for downstream analyses. Three statistical analyses were performed separately for each clone: (i) each of the $KRAS^{MUT}$ condition ($n = 2$) was tested against two $KRAS^{WT}$ controls ($n = 4$); data were prefiltered to contain at least two valid values in each condition tested; this analysis was used to find mutant-specific signatures, (ii) all samples from the $KRAS^{MUT}$ conditions ($n = 14$) were tested against $KRAS^{WT}$ controls ($n = 4$); data were prefiltered to contain at least three valid values in each condition tested; this analysis was used to find pan-mutant signatures, and (iii) all samples from the 'DVR' subtype ($KRAS^{G12D}$, $KRAS^{G12V}$, and $KRAS^{G12R}$; $n = 6$) and 'Other' subtype ($KRAS^{G12C}$, $KRAS^{G13C}$, $KRAS^{Q61H}$, $KRAS^{Q61R}$; $n = 8$) were tested against $KRAS^{WT}$ controls ($n = 4$); data were prefiltered to contain at least three valid values in each condition tested; this analysis was used to find DVR signatures.

Fixed-effect ANOVA variance partitioning

To quantify the relative contributions of parental cell line, clone background, *KRAS* genotype, and clone-dependent genotype responses to molecular variation, we performed a fixed-effects ANOVA variance-partitioning analysis across the transcriptomic, proteomic, and phosphoproteomic datasets using R packages lm and ANOVA. Complete-case filtering was performed independently within each omics layer using the retained samples for that layer (RNA, proteome, or phosphoproteome). Gene symbols were extracted from the annotations of complete-case RNA, proteome, and phosphoproteome features. A cross-omics matched gene set was then defined as the intersection of genes represented in all three complete-case datasets. For the phosphoproteome, all complete-case phosphosites linked to matched genes were retained, allowing multiple phosphosites to be associated with the same gene or protein.

Before cross-omics matching, the complete-case RNA dataset contained 13,002 feature rows representing 12 994 unique genes. The complete-case proteome dataset contained 5,961 protein rows representing 5,974 unique mapped genes, and the phosphoproteome dataset contained 14,257 phosphosites representing 2,867 unique mapped genes. The final matched dataset included 2338 genes represented across all three omics layers, corresponding to 2,338 RNA rows, 2,338 proteome rows, and 12,913 phosphosites. For each retained feature, normalized molecular abundance was modelled using the following fixed-effects ANOVA:

$$\text{Value} \sim \text{Cell line} + \text{Clone} + \text{Allele} + \text{Clone} : \text{Allele}$$

The Cell_line term captured differences between the KP4 and 8988T parental cell line backgrounds, while the Clone term captured baseline differences among clones after accounting for the parental cell line. The Allele term captured the shared mutant effect across clone backgrounds, whereas the Clone:Allele interaction captured context-specific clone responses to *KRAS* genotype. Residual variation

represented replicate-level variability and variation not explained by the included model terms. For each feature, the variance proportions were calculated and summarized across features within each omics layer.

Identification of pan-mutant and mutant-selective KRAS signatures

Following differential expression analysis, each gene, protein, or phosphosite was assigned a score of +1 or −1 per cell line depending on whether it met the statistical significance threshold and the direction of regulation. Scores were then summed across cell lines to generate an overall score for each feature, which was subsequently used to define KRAS signatures. For the pan-mutant KRAS, DVR, and Other signatures, candidate hits were defined as upregulated (overall score ≥ 2) or downregulated (overall score ≤ -2) in at least two of the four cell lines. To identify mutant-selective signatures, a gene, protein, or phosphosite was determined as specific to a given KRAS mutant if it (i) was consistently differentially expressed in at least two clones of that allele, with the sign of the score reflecting directionality, and (ii) was present in no more than one clone of the other alleles.

Enrichment analysis

A multiple gene list enrichment analysis was performed using the Metascape web interface (https://metascape.org) [29] to perform functional enrichment analysis against a custom background gene set consisting of unique genes/proteins/phosphoproteins included in the corresponding statistical analysis. Over-representation analysis of selected signature gene sets was performed using the phyper() function in R. The following sets were used: (i) the KRAS-dependence gene set based on Klomp *et al.* [10], (ii) the KRAS Hallmarks genes set based on the MSigDB [30], (iii) the 1-h and 24-h ERK-dependent KRAS phosphoproteome based on Klomp *et al.* [11], and (iv) the core KRAS signalling signature based on Kabella *et al.* [12].

Kinase motif enrichment analysis

Phosphoproteomics datasets were filtered to include only peptides with a single site of phosphorylation. Enriched motifs in sites significantly upregulated or downregulated in at least two clones within the pan-KRAS^{MUT} group, 'DVR' KRAS group, or two 'Other' KRAS mutant group compared to matched KRAS^{WT}-expressing cells were identified using the phosphoproteomic enrichment analysis tool (kinase-library.mit.edu) with predetermined foreground and background sets. Sites were called as conforming to a motif if their percentile rank was within the top 15 Ser-Thr kinases or the top 8 Tyr kinases, and enrichment *P*-values were adjusted by the Benjamini-Hochberg procedure.

Data visualization

Hierarchical clustering analysis and heatmap visualization were performed using the R package pheatmap (1.0.13). UpSet plots were generated using the R package UpSetR (1.4.0). Correlation plots were generated using the R package corrplot (0.95). Barplots were generated using the R package ggplot2 (3.5.2).

Results

Derivation of isogenic cell models to study mutant KRAS variants in pancreatic ductal adenocarcinoma

We previously demonstrated that a subset of PDAC cells can rewire signalling to survive KRAS ablation [13]. Importantly, these KRAS-independent cells demonstrated phenotypic reversibility in morphology, growth kinetics, and signalling when mutant KRAS was re-expressed, providing a tractable and genetically controlled platform to dissect the molecular consequences of specific *KRAS* mutations systematically in PDAC cells [13]. We employed a similar CRISPR/Cas9-based gene-editing strategy to ablate *KRAS* expression in two human PDAC cell lines (8988T and KP4). Single cell subclones were expanded and screened for successful *KRAS* ablation by immunoblotting (Supplementary Fig. S1A and B). Next, we selected two KRAS-deficient clones per parental cell line (8988T K275 and K328 and KP4 K22 and K63) (Supplementary Fig. S1C). Whole exome-sequencing did not identify recurrent SNVs nor CNVs in cancer drivers that would be predicted to endow KRAS independence (Supplementary Tables S1–S3), suggesting that these cell lines are suitable for isogenic comparisons of mutant KRAS variants. Nonetheless, the clones differed in baseline measures of canonical downstream signalling pathways: mitogen-activate protein kinase (MAPK; pERK) and PI3K (pAKT) (Supplementary Fig. S1C and D). We reconstituted these clones with WT or seven common mutant *KRAS* variants co-expressed with a GFP reporter by lentiviral transduction, selecting for similar KRAS expression by fluorescent-activated cell sorting (Fig. 1A). Importantly, we confirmed comparable KRAS expression levels by immunoblotting (Fig. 1B). This controlled expression enabled direct comparisons across KRAS mutants within each cellular background, ensuring that observed differences reflect mutant-specific biology rather than variability in protein expression.

Multi-omic profiling of KRAS mutations in isogenic human pancreatic ductal adenocarcinoma cell lines

To determine the molecular effects of mutant KRAS expression in PDAC cells, we quantified the steady-state transcriptome, proteome, and phosphoproteome across all four isogenic cell line series *via* RNA-Seq and DIA-MS-based proteomics analyses. Multi-omics profiling confirmed deep coverage of the transcriptome, proteome, and phosphoproteome: RNA-Seq identified, on average, transcripts of over 14,000 protein-coding genes, while DIA-MS identified more than 7,500 unique protein groups across all samples (Supplementary Fig. S2A and B). Similarly, between 35,000 and 40,000 unique class-I phosphosites [25] were detected across all samples, with the exception of K22 KRAS^{G13C}, which yielded ∼17,000 sites (Supplementary Fig. S2C). The lower phosphosite coverage in this sample likely resulted from a small sample input, as a repeat biologic replicate identified ∼37,000 sites but showed a batch effect during data integration (Supplementary Fig. S2C and D). As a result, this sample was excluded from downstream phosphoproteomic analyses.

We performed several assessments to validate the quality of the multi-omic data for mutant KRAS comparisons. First, KRAS expression was comparable across all samples in the proteomics data (Supplementary Fig. S3A), consistent with immunoblotting results (Fig. 1B). Second, the average absolute correlation between the replicates in the proteome and phosphoproteome dataset was $\rho = 0.99$ and $\rho = 0.93$, respectively, demonstrating excellent technical reproducibility (Supplementary Fig. S3B). Third, we assessed concordance between omic layers. Pairwise Spearman correlation analysis revealed a moderate positive relationship ($\rho = 0.45$–0.65 across samples) between mRNA and protein expression changes across KRAS variants (Supplementary Fig. S3C), indicating that a considerable proportion of proteomic variation mirrors transcriptomic changes in steady-state conditions. Similar mRNA-protein level correlations have been observed widely in other studies independent of the cell

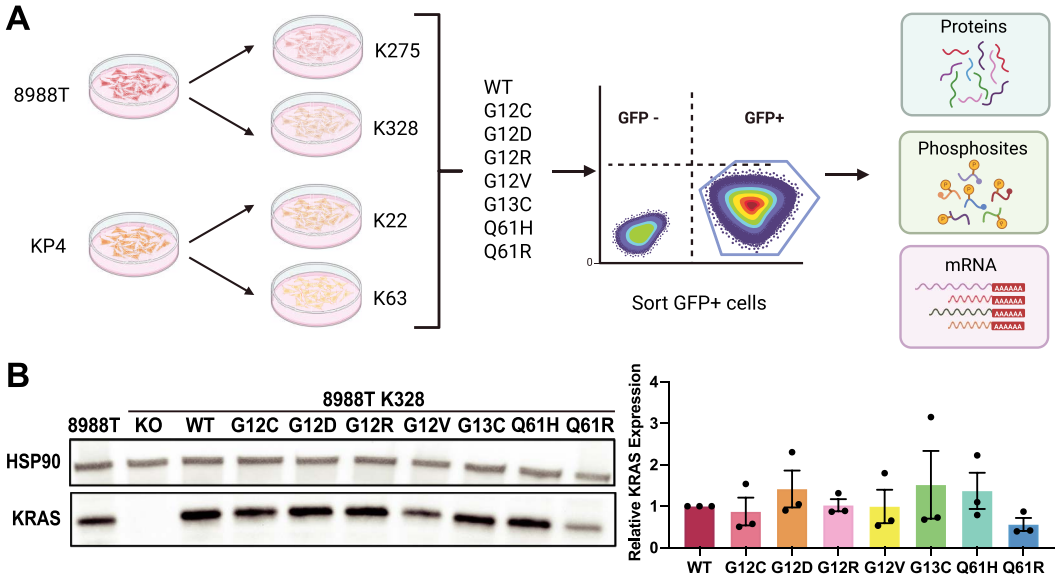


Figure 1 Generation and molecular profiling of isogenic *KRAS* mutant PDAC cells. (A) Experimental workflow of multi-omics profiling (RNA-seq, DIA-MS proteome, and phosphoproteome) of two *KRAS* KO clones derived from each parental PDAC cell line (8988T and KP4) reconstituted with WT or seven different KRAS mutants to assess KRAS-dependent molecular changes. KRAS was co-expressed with GFP, which was used for sorting cells of similar fluorescence. Created in BioRender. Muzumdar, M. (2026) https://BioRender.com/9a470xf. (B) Representative immunoblot and quantification of relative KRAS protein expression (mean ± SEM of $n = 3$ biological replicates) of each mutant (*versus* WT, normalized to loading control HSP90) showing comparable KRAS expression across reconstituted 8988T K328 cells. KRAS expression was not significantly different to WT (repeated measures one-way ANOVA with Dunnett's *post hoc* test).

lines analysed [31]. Protein-phosphosite correlations also revealed a moderate positive relationship between both layers ($\rho = 0.45$–0.61) (Supplementary Fig. S3C), consistent with previous reports [21]. Therefore, these data provide a rigorous, high-quality, and comprehensive molecular resource to study KRAS mutant- and allele-specific pathway engagement in PDAC cells.

Defining molecular signatures of KRAS mutation

To evaluate how mutant KRAS ($KRAS^{MUT}$) variants differentially affect PDAC cells, we first performed unsupervised hierarchical clustering for each independent omics layer (Fig. 2A). Although mutant KRAS-expressing cells largely clustered away from WT KRAS ($KRAS^{WT}$) within each cell line, there were no consistent global clustering patterns for specific mutant alleles across the mRNA, proteome, and phosphoproteome layers. Furthermore, cell line identity, rather than mutant KRAS expression, was the primary driver of molecular variability across samples and omics layers, even separating clones derived from the same parental background (Fig. 2A). Interestingly, differential expression analyses revealed a spectrum of responsiveness to $KRAS^{MUT}$ reconstitution across cell lines. 8988T K275 displayed the most pronounced transcriptomic, proteomic, and phosphoproteomic changes, while 8988T K328 showed minimal changes and KP4-derived clones exhibited an intermediate response (Fig. 2B). We observed a similar pattern of cell-specific responsiveness in PI3K and especially MAPK signalling when analysed by immunoblotting (Fig. 2C), arguing that these canonical pathways may, in part, govern the differential impacts of $KRAS^{MUT}$ expression on individual cell lines.

To quantify the sources of molecular variation, we performed fixed-effect ANOVA variance partitioning across each omics layer (Supplementary Fig. S4). Across features, cell line identity showed the largest median variance contribution in the transcriptome (56.6%), proteome (49.0%), and phosphoproteome (23.1%), with clone identity representing the second largest contributor (medians of 17.7%–23.9%). In contrast, KRAS allele identity accounted for only a small fraction of the observed molecular variance (medians of 3.3%–5.3%), while clone-by-mutant interactions explained a modest but consistently larger proportion of variance than mutant identity alone across each omics layer (medians of 8.5%–14.8%). These findings argue that the molecular consequences of KRAS allele expression on the cellular transcriptome, proteome, and phosphoproteome are strongly influenced by the cellular context in which they are expressed.

We next derived a steady-state $KRAS^{MUT}$ signature by selecting features consistently differentially expressed when comparing all $KRAS^{MUT}$ variants relative to $KRAS^{WT}$ in at least two of the four cell lines, thereby enriching for changes that are not clone-specific but reflect shared $KRAS^{MUT}$-dependent programmes. Using a FDR threshold of 0.05 and an absolute fold-change cutoff of 1.3, the resultant $KRAS^{MUT}$ transcriptomic signature was comprised of 233 upregulated and 456 downregulated genes (Supplementary Table S4). Similarly, differential expression analysis of proteomic data defined a $KRAS^{MUT}$ signature of 277 upregulated and 298 downregulated proteins, mirroring the extent of reprogramming observed at the transcriptomic level (Supplementary Table S4). At the phosphoproteome level, we identified 1050 upregulated and 621 downregulated phosphosites, assigned to 531 and 298 distinct phosphorylated proteins, respectively (Supplementary Table S4).

We next performed enrichment analysis to identify hallmark pathways, processes, and kinases systematically altered by $KRAS^{MUT}$ expression across the transcriptome, proteome, and phosphoproteome. Across functional pathways, we observed substantial overlap at the mRNA and protein levels, with notable differences in directionality and strength of enrichment (Fig. 3A and Supplementary Fig. S5).

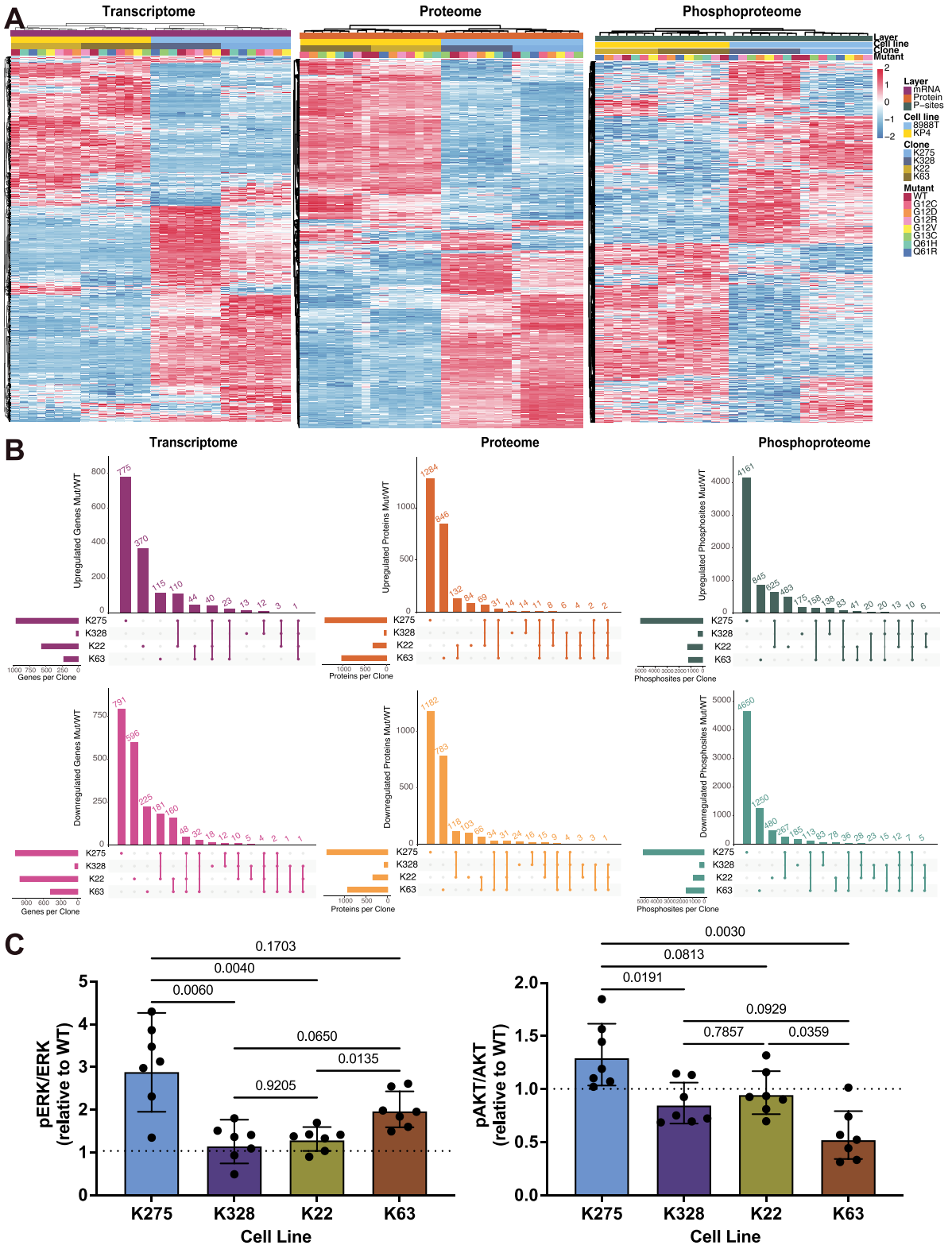


Figure 2 Baseline cellular state dictates the impact of mutant KRAS expression. (A) Unsupervised hierarchical clustering of transcriptomic, proteomic, and phosphoproteomic datasets show that clone origin, not *KRAS* allele, is the major driver of sample segregation, even between clones derived from the same parental line. Colour scale denotes row-normalized absolute abundance. (B) UpSet plots showing the overlap of significantly upregulated (top) and downregulated (bottom) genes (transcriptome), proteins (proteome), and phosphosites (phosphoproteome) across all four reconstituted cell lines. A fold change $\geq$1.3 and adjusted *P*-value $\leq$.05 threshold were used to determine differential expression of all $KRAS^{MUT}$ relative to $KRAS^{WT}$ for at least two cell lines. Each bar represents the number of shared or unique differentially expressed features between clones. Shared upregulated and downregulated features highlight the limited global convergence of KRAS-dependent molecular responses across cell lines. (C) Quantification of pERK1/2 (T202/Y204) and pAKT (S473) levels relative to total ERK and AKT levels in each cell line. The ratios (geometric means $\pm$ geometric SD) of the expression $KRAS^{MUT}$ ($n=7$ mutants) relative to $KRAS^{WT}$ (average of $n=3$ biologic replicates) for each cell lines are shown. *P*-values are derived from Brown-Forsythe lognormal ANOVA with games-Howell's *post hoc* test.

The strongest convergent association we observed for both the transcriptome and proteome across functional databases was downregulation of interferon signalling response ['interferon alpha' and 'gamma response' in the Molecular Signatures Database (mSigDB) Hallmark gene sets, 'interferon signalling' and 'interferon alpha/beta signalling' in Reactome Pathways, and 'negative regulation of viral genome replication' in Gene Ontology (GO): Biological Processes] with $KRAS^{MUT}$ (Fig. 3A and Supplementary Fig. S5). Strikingly, mitochondrial translation-related proteins (GO: Biological Processes and Reactome Pathways) were strongly and uniquely enriched in the upregulated proteome (Supplementary Fig. S5). To gain insights into additional signalling events altered in $KRAS^{MUT}$ PDAC cell lines, we performed kinase motif enrichment analysis (KMEA) [32] using the $KRAS^{MUT}$ phosphoproteomic signature. We observed strong enrichment for upregulated sites conforming to the ERK1/2 motif as well as motifs for other related MAPKs (JNK and p38) and cyclin-dependent kinases (CDKs) (Fig. 3B). Conversely, we observed a distinct DYRKs signature among the downregulated sites (Fig. 3B). Together, our multi-omics $KRAS^{MUT}$ signatures provide a resource for defining the convergent effects of $KRAS^{MUT}$ expression in reconstituted PDAC cells.

Towards a unified multi-omic mutant KRAS signature across datasets

The suppression of interferon response signalling and inferred enrichment of increased ERK1/2 activity and reduced DYRK activity mirrored findings from recent studies on the ERK-dependent transcriptome and phosphoproteome [10, 11]. Therefore, we sought to rigorously compare our $KRAS^{MUT}$ transcriptomic signature against publicly available KRAS-dependent signatures to assess concordance and biological relevance. As a benchmark, we used the widely adopted Hallmark KRAS Signalling gene sets from the MSigDB, a reference standard for defining KRAS pathway engagement across cancers [30]. To quantify enrichment, we performed over-representation analysis of the selected gene sets, stratifying by direction of regulation (UP or DOWN). When comparing our upregulated $KRAS^{MUT}$ transcriptomic signature with the Hallmark KRAS Signalling UP signature, we observed significant overlap (enrichment = 8.48, $P = 1.09 \times 10^{-12}$; Fig. 4A). Likewise, our downregulated $KRAS^{MUT}$ transcriptomic signature also showed significant enrichment with the Hallmark KRAS Signalling DOWN gene set (enrichment = 3.37, $P = 4.39 \times 10^{-4}$; Fig. 4A). Despite this enrichment, only 19 and 11 specific genes overlapped between ours and the Hallmark UP and DOWN gene sets, respectively (Supplementary Table S5). We reasoned that this may be due to the broad, pan-cancer derivation of the Hallmark gene sets using immortalized lung, breast, kidney, and prostate epithelial cells [30], whereas our signature captures PDAC-specific transcriptional programmes induced by $KRAS^{MUT}$. Therefore, we compared our results with the KRAS-dependent transcriptome reported by Klomp *et al.* [10] and derived from eight human *KRAS* mutant PDAC cell lines following a 24-h *KRAS* siRNA treatment. Despite significant enrichment between our upregulated (enrichment = 5.64, $P = 6.41 \times 10^{-23}$; Fig. 4A) and downregulated (enrichment = 3.37, $P = 2.07 \times 10^{-19}$; Fig. 4A) $KRAS^{MUT}$ transcriptomes, the number of overlapping genes (48 and 79, respectively; Supplementary Table S5) remained modest as compared to the total number of significantly altered mRNAs we detected. The partial overlap may be explained by differences in experimental design, as our dataset represents steady-state molecular profiles, whereas Klomp *et al.* measured acute transcriptional responses to KRAS suppression. Importantly, only a small number of genes ($n = 12$) overlapped across all datasets (*CELSR2*, *DUSP6*, *ETV4*, *ETV5*, *GPRC5C*, *HBEGF*, *LIF*, *MALL*, *MX1*, *SPRY2*, *SYNPO*, and *TMEM158*; Supplementary Table S5), including many genes previously described as being transcriptionally regulated by MAPK signalling [33]. Given this sparse overlap, cellular context largely overshadows the effect of *KRAS* mutation across cell lines.

We then compared our $KRAS^{MUT}$ proteomic signature against the Hallmark KRAS Signalling and Klomp *et al.* datasets (Fig. 4B). The upregulated $KRAS^{MUT}$ proteome also showed significant enrichment with Hallmark KRAS Signalling UP (enrichment = 2.07, $P = 3.63 \times 10^{-2}$), while the downregulated proteome exhibited stronger enrichment with the corresponding DOWN gene set (enrichment = 5.25, $P = 7.65 \times 10^{-4}$; Fig. 4B). Comparison with the Klomp *et al.* signatures yielded more restricted overlap, with the upregulated proteome showing a weaker enrichment (enrichment = 1.53, $P = 2.21 \times 10^{-2}$) and the downregulated proteome displaying more significant enrichment (enrichment = 2.54, $P = 1.36 \times 10^{-8}$; Fig. 4B). The lower overlap at the proteomic level is not unexpected, given that both reference datasets were generated from transcriptomic data and that there is moderate correlation between mRNA and protein abundance (Supplementary Fig. S2C) [34]. Furthermore, only two genes (*SYNPO* and *MX1*) were consistently downregulated at both the transcriptomic and proteomic layers across all datasets (Supplementary Table S5).

Lastly, we compared our $KRAS^{MUT}$ phosphoproteomic signature against two recently reported reference phosphoproteomics datasets (Fig. 4C): (i) the ERK-regulated phosphoproteome identified by Klomp *et al.* [11] following acute (1-h) and prolonged (24-h) ERK inhibition, and (ii) the curated KRAS core phosphoproteome described by Kabella *et al.* [12] after a 2-h KRAS inhibitor treatment across three established PDAC cell lines. We observed strong enrichment of our $KRAS^{MUT}$ upregulated phosphoproteome with the ERK-regulated phosphoproteome [11] at both 1-h (enrichment = 4.55, $P = 2.2 \times 10^{-30}$) and 24-h (enrichment = 2.84, $P = 6.1 \times 10^{-34}$) timepoints, as well as with the Kabella *et al.* [12] KRAS Core Signature (enrichment = 6.44, $P = 1.46 \times 10^{-18}$; Fig. 4C). Notably, we observed strong overlap of upregulated ($n = 85$) and downregulated ($n = 53$) phosphoproteins compared to the Klomp *et al.* [11] 24-h ERK-regulated dataset, likely reflecting greater convergence of the long-term perturbation with our steady-state conditions. Likewise, our $KRAS^{MUT}$ downregulated phosphoproteome signature showed significant enrichment with the Klomp *et al.* (24-h) dataset (enrichment = 2.10, $P = 1.53 \times 10^{-8}$) but no significant enrichment with the Klomp *et al.* (1-h) dataset ($P = 7.64 \times 10^{-2}$). Despite significant overlap in pairwise comparisons, across all datasets, ERBB2 (S1054) was the only phosphosite consistently downregulated, underscoring the narrow shared KRAS-dependent phosphoproteomic core signature across the studies (Supplementary Table S5).

Comparative analysis between common pancreatic ductal adenocarcinoma KRAS mutations and other variants

Given that $KRAS^{G12D}$, $KRAS^{G12V}$, and $KRAS^{G12R}$ represent the most prevalent *KRAS* mutations in PDAC and have been associated with distinct biochemical properties [4] and clinical outcomes [2, 35, 36], we next sought to determine how their molecular profiles compare to those of less frequent alleles. We hypothesized that the molecular programmes for $KRAS^{G12D}$, $KRAS^{G12V}$, and $KRAS^{G12R}$ (DVR) would converge more strongly, suggesting an ideal cellular state that is compatible with PDAC development. We stratified our

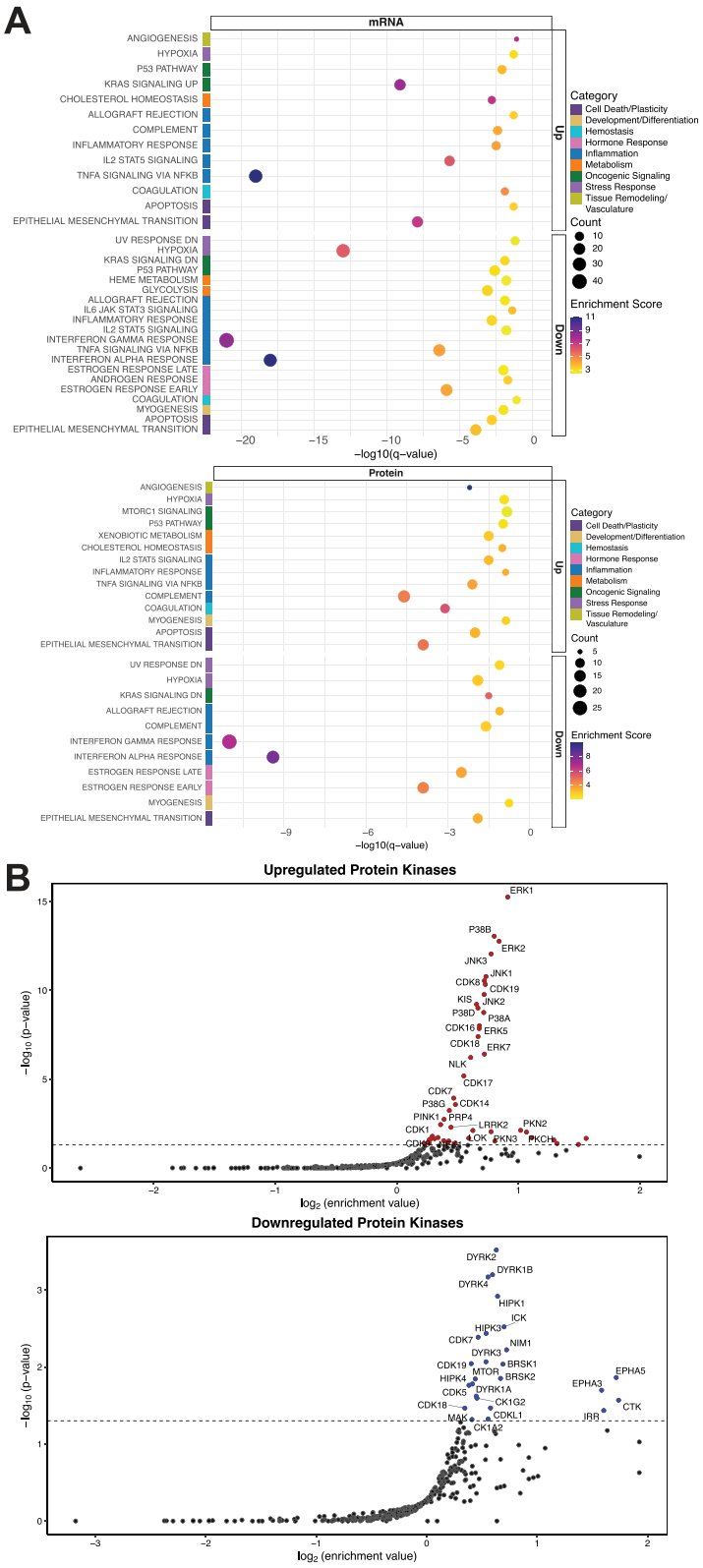


Figure 3 Functional pathways and kinase activity associated with mutant KRAS expression. (A) Pathway-level enrichment using the mSigDB hallmarks dataset for the transcriptomic (mRNA) and proteomic (protein) differences [upregulated (up) or downregulated (down)] for the $KRAS^{MUT}$ multi-omic signatures defined by selective differentially expressed hits (FC $\geq$ 1.3 and FDR $\leq$ 0.05) in at least two out of four clones ($\geq$2 clones) compared to $KRAS^{WT}$. Colour scale denotes enrichment score. Circle size designates gene count overlap. $-\log_{10}$(*q*-value) of hypergeometric test is plotted. (B) KMEA using phosphosites in the $KRAS^{MUT}$ multi-omic signature reveals increased phosphorylation of ERK1/2 kinase substrates (upregulated protein kinases) and decreased phosphorylation DYRK kinase substrates (downregulated protein kinases). Log_2 enrichment *versus* $-\log_{10}$(*P*-value) is plotted.

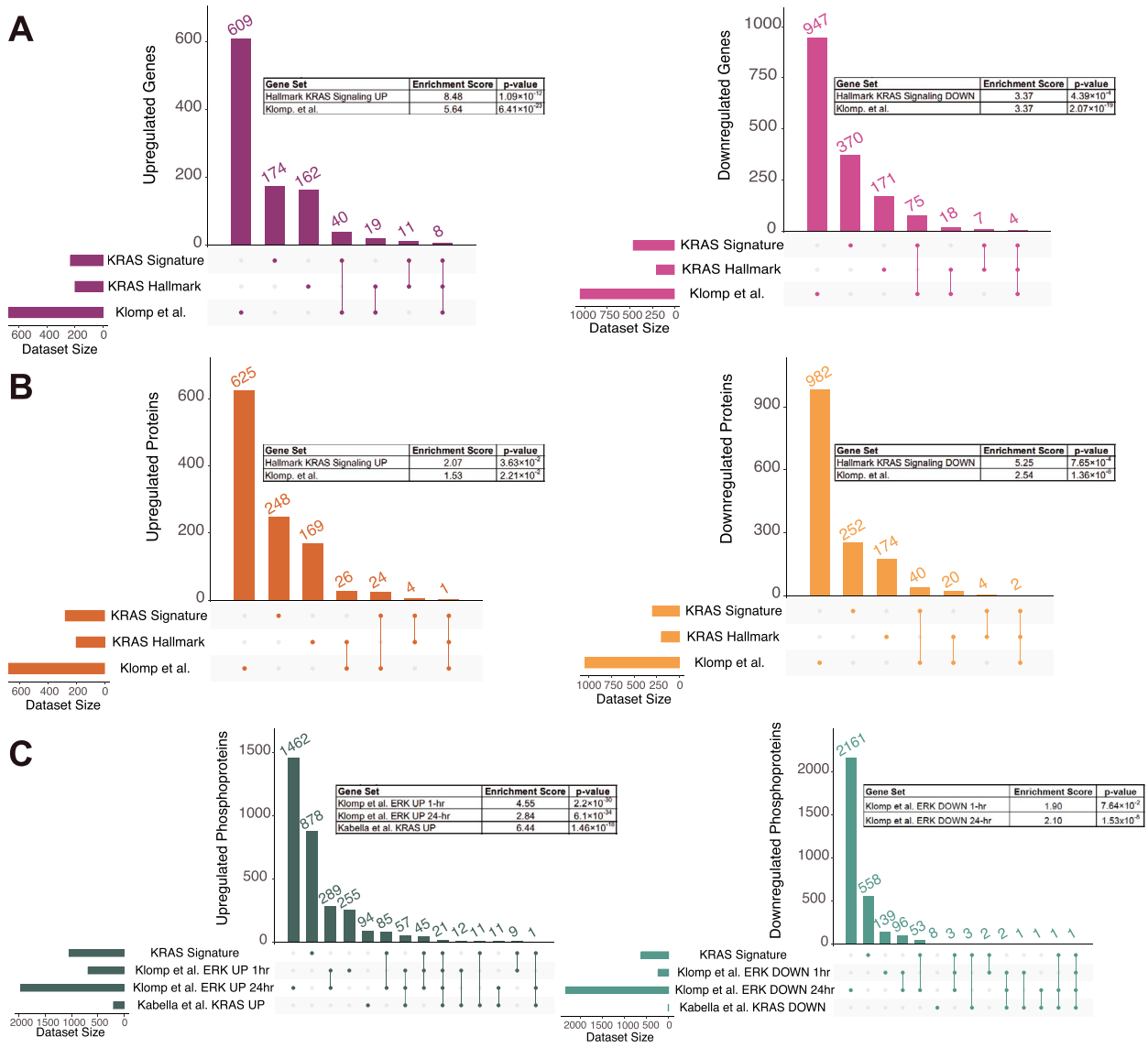


Figure 4 The KRAS^{MUT} multi-omic signatures significantly overlap with prior KRAS-dependent datasets. (A) UpSet plot illustrating overlap between the transcriptomic KRAS^{MUT} signature and previously published transcriptomic KRAS-dependent signatures (Hallmark KRAS signalling [30] and Klomp *et al.* [10]) identifies a small core of shared KRAS-regulated genes. Enrichment scores and *P*-values of hypergeometric test are shown for corresponding upregulated or downregulated gene sets. (B) UpSet plot illustrating overlap between the proteomic KRAS^{MUT} signature proteomic and previously published KRAS-dependent transcriptomic signatures shows moderate overlap with KRAS-regulated datasets (Hallmark KRAS signalling [30] and Klomp *et al.* [10]) enrichment scores and *P*-values of hypergeometric test are shown for corresponding upregulated or downregulated gene sets. (C) UpSet plot illustrating overlap between the phosphoproteomic KRAS^{MUT} signature strong enrichment despite limited share sites with 1-h and 24-h ERK-regulated phosphoproteome and KRAS phosphoproteome core signature (Klomp *et al*. [11] and Kabella *et al*. [12]). Enrichment scores and *P*-values of hypergeometric test are shown for corresponding upregulated or downregulated gene sets.

analysis by grouping DVR separately from the remaining KRAS variants (Other) and performed differential expression analysis relative to their isogenic KRAS^{WT} counterparts. Contrary to our hypothesis, we observed significant overlap between the upregulated and downregulated multi-omics signatures comparing DVR *versus* Other (Fig. 5A). Functional enrichment analysis similarly showed a high degree of overlap between DVR and Other signatures across both the transcriptome and proteome, including suppression of interferon signalling responses (Fig. 5B). Furthermore, KMEA revealed upregulation of ERK1/2 and other MAPK family site motifs across both DVR and Other phosphoproteomic signatures (Fig. 5C). As before, DYRK kinase substrates were consistently downregulated in both groups, with this effect being more pronounced in the other mutants compared to the DVR signature (Fig. 5D). In contrast, DVR downregulated sites—but not Other downregulated sites—were enriched for motifs corresponding to AMPK-related kinases downstream of the LKB1 tumour suppressor (BRSK, SIK, and MARK family kinases) (Fig. 5D). Together, these data reveal that transcriptomic, proteomic, and phosphoproteomic impacts largely converge irrespective of allele frequency in PDAC, arguing against a specific cell state induced by common KRAS variants in PDAC.

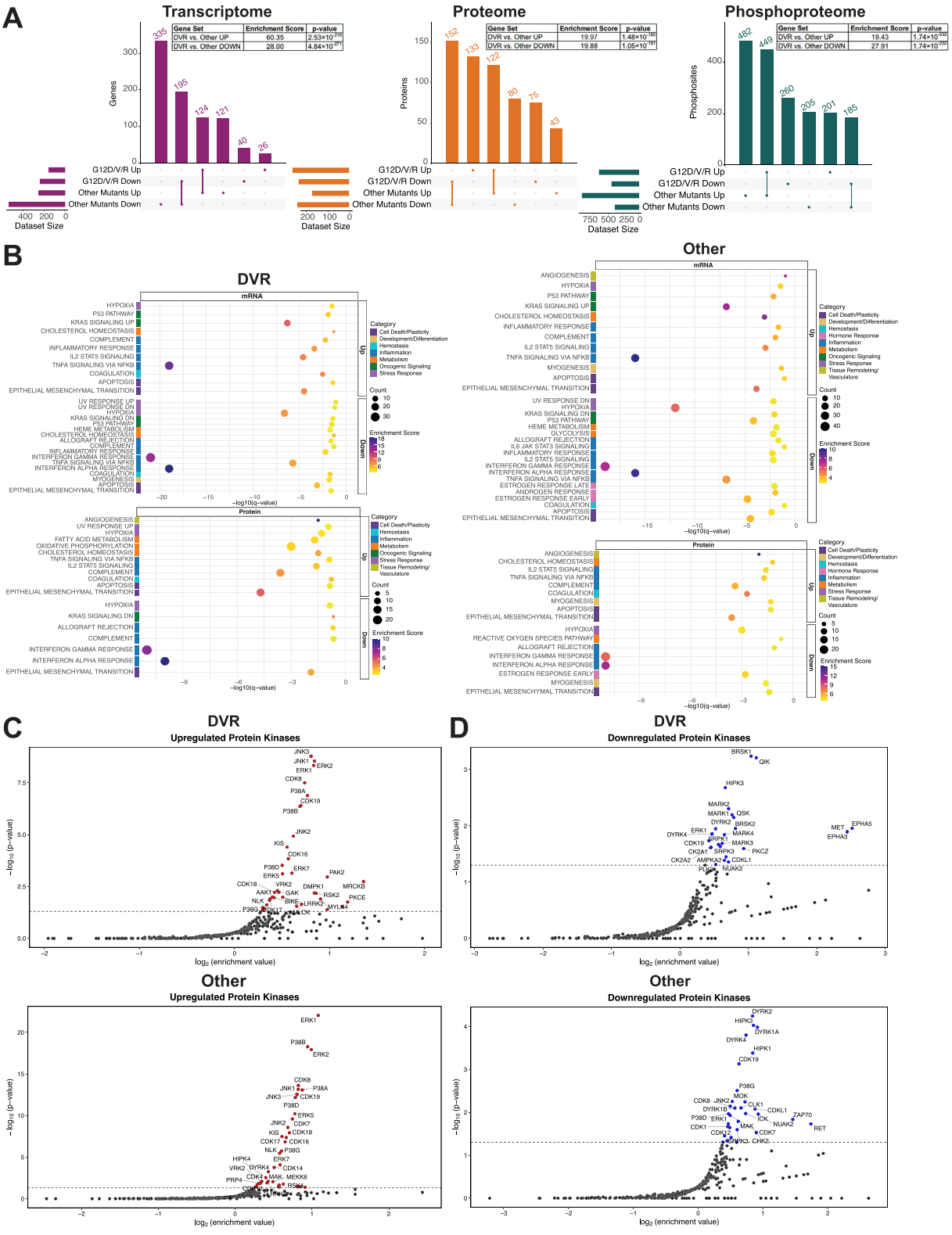


Figure 5 Comparison of common *versus* less common KRAS variants in PDAC. (A) UpSet plot illustrating overlap between the multi-omic signatures of DVR ($KRAS^{G12D}$, $KRAS^{G12V}$, and $KRAS^{G12R}$) and other ($KRAS^{G12C}$, $KRAS^{G13C}$, $KRAS^{Q61R}$, and $KRAS^{Q61H}$) KRAS variants. Enrichment scores and *P*-values of hypergeometric test are shown for corresponding upregulated (UP) or downregulated (DOWN) gene sets. (B) Pathway-level enrichment using the mSigDB hallmarks dataset for the transcriptomic (mRNA) and proteomic (protein) differences [upregulated (up) or downregulated (down)] for the DVR and other multi-omic signatures each compared to $KRAS^{WT}$. Colour scale denotes enrichment score. Circle size designates gene count overlap. $-\log_{10}$(*q*-value) of hypergeometric test is plotted. (C) KMEA using phosphosites in the DVR and other multi-omic signatures reveals increased phosphorylation of ERK1/2 kinase substrates (upregulated protein kinases). Log_2 enrichment *versus* $-\log_{10}$(*P*-value) is plotted. (D) KMEA using phosphosites in the DVR and other multi-omic signatures shows decreased phosphorylation if DYRK kinase substrates (downregulated protein kinases) for both signatures. AMPK-related kinases downstream of the LKB1 tumour suppressor (BRSK, SIK, and MARK family kinases) were uniquely downregulated in the DVR signature. Log_2 enrichment *versus* $-\log_{10}$(*P*-value) is plotted.

Evaluation of KRAS mutant-selective signatures in pancreatic ductal adenocarcinoma

To uncover *KRAS* allele-specific biology in our datasets, we next focused on identifying mutant-selective signatures. After defining differentially expressed candidates relative to $KRAS^{WT}$ for each KRAS mutant in each cell line, we classified them as mutant-selective if they were upregulated or downregulated in at least two of the four clones (score ≥ 2 or ≤ -2, respectively) for that mutant, while being differentially expressed in no more than one clone of all the other mutants (score ≤ 1 or ≥ -1). We visualized these candidate features (genes, proteins, or phosphosites) using heatmaps to assess whether allele-specific patterns emerged. Strikingly, the majority of allele-specific candidates showed similar directional change in candidate abundance with the other mutants such that no consistent mutant-specific transcriptomic, proteomic, or phosphoproteomic signatures stood out (Fig. 6A). Even for $KRAS^{Q61R}$, which harboured the most mutant-selective candidates, the change in abundance for other mutants (relative to $KRAS^{WT}$) largely trended in the same direction (Fig. 6B), revealing that these candidate features (genes, proteins, and phosphosites) were not exclusively enriched in $KRAS^{Q61R}$-expressing cells. Consistent with this, supervised hierarchical clustering did not show specific clustering of Q61R across cell lines for $KRAS^{Q61R}$ mutant-selective candidates (Fig. 6C), indicating that these candidate features are not truly $KRAS^{Q61R}$-specific. Together, these findings suggest that cellular context (baseline gene expression and signalling networks), rather than intrinsic allele-specific properties, predominantly governs the molecular impact of KRAS mutations, thereby overriding subtle mutant-specific differences.

Discussion

In this study, we established an isogenic human PDAC cellular system to systematically interrogate the molecular consequences of seven different KRAS mutations on the transcriptome, proteome, and phosphoproteome. By restoring comparable KRAS expression in *KRAS*-deficient KO clones, we created a platform that enabled direct allele-to-allele comparisons. Multi-omics profiling, while achieving excellent technical reproducibility, revealed that baseline cellular state, rather than intrinsic allele identity, was the predominant driver of variation in molecular signatures for our reconstituted PDAC cell lines (Supplementary Fig. S6). Overall, our datasets based on isogenic cells provide a high-quality multi-omic reference resource on the molecular impacts of common *KRAS* mutant variants in cancer.

A key strength of our approach is the ability to directly compare multiple KRAS alleles under controlled expression levels, minimizing confounding effects from variable KRAS abundance. However, a limitation of our system is that, by design, it relies on PDAC cell lines that have undergone signalling rewiring to survive in the absence of KRAS. It is therefore possible that KRAS plays a less dominant role in this context, contributing to the lack of global convergence across clones. Moreover, while our approach enables the simultaneous comparison of a broader panel of KRAS mutants, the limited number of clones analysed and the usage of *in vitro* cancer cell culture models may constrain our resolution to detect more subtle allele-specific effects. This interpretation aligns with prior reports of nuanced allele-specific differences, such as the inability of $KRAS^{G12R}$ to regulate micropinocytosis [8]. Nonetheless, macropinocytosis occurs even in $KRAS^{G12R}$-expressing cells, arguing that compensatory, KRAS-independent pathways may sustain core cellular programmes, thereby minimizing mutant-specific divergence.

To determine the generalizability of our method to define core KRAS-regulated pathways, we compared our $KRAS^{MUT}$ signature with available KRAS reference signatures [10–12, 30]. Our transcriptomic $KRAS^{MUT}$ programme showed modest overlap with the Hallmark KRAS gene set [30] and the KRAS-targeted siRNA-derived signatures of Klomp *et al.* [10], differences likely reflecting both the pan-cancer derivation of the Hallmark set and the acute perturbation design of the Klomp study when compared to our steady-state conditions in PDAC. Importantly, proteomic-level overlap was even more restricted, a finding that likely stems from biological factors—such as the imperfect correlation between mRNA and protein abundance—and differences in analytical sensitivity between RNA-Seq and DIA-MS platforms [21, 31]. These results highlight that only limited KRAS-regulated core features are consistently maintained. Consistent with this, it has been postulated that specific KRAS mutants induce a 'sweet spot' of signalling alterations to induce a cell state optimized for tumour development and maintenance in specific tissues [37]. Indeed, the prevalence of $KRAS^{G12R}$ mutation exceeds the predicted frequency in PDAC [38], indicating that mutant-specific oncogenic signalling outputs may provide a selective advantage in a context-specific matter. However, contrary to this 'Goldilocks' hypothesis, common (DVR) and uncommon (Other) mutants largely converged on regulating the same signalling pathways and transcriptional outputs in our cells. Importantly, our reconstituted *in vitro* system captures steady-state molecular outputs but does not recapitulate the microenvironmental and evolutionary pressures that may differentially select for specific *KRAS* alleles during *in vivo* tumour development [39–41]. Therefore, the convergence observed under these conditions does not necessarily contradict the Goldilocks hypothesis, nor does it exclude allele-specific functional differences or fitness advantages that may emerge under *in vivo* selective pressures.

Pathway-level enrichment revealed that mutant KRAS expression suppressed interferon response genes at the transcriptome and proteome level, a finding that is consistent with previous reports of KRAS-mediated immune evasion in PDAC via suppression of type I interferon responses [42]. At the phosphoproteome level, inferred ERK1/2 activity was consistently enriched across all KRAS mutants, whereas DYRK motif substrates were broadly suppressed. Our results align with a recent study that suggested that DYRK phosphosite motifs are upregulated as a compensatory response to sustained ERK inhibition in PDAC, colorectal cancer (CRC), and non-small cell lung cancer (NSCLC) models [11]. Therefore, KRAS-induced MAPK signalling may suppress DYRK activity, however the precise mechanisms by which this occurs and whether DYRK signalling might enable bypass to KRAS inhibition remains to be elucidated.

Finally, attempts to identify mutant-specific signatures revealed that few transcripts, proteins, or phosphoproteins could be uniquely attributed to a single allele. These findings suggest that intrinsic allele-specific programmes are modest in magnitude and are often overridden by baseline cell state. Although our analyses did not reveal robust allele-specific molecular signatures, prior clinical [2, 35, 36] and *in vivo* [39–41] studies have reported functional distinctions among KRAS mutants. However, recent evidence also suggests that these differences may be context-dependent rather than intrinsic. For instance, 3D histological reconstruction and genetic mapping of low-grade pancreatic intraepithelial neoplasia (PanINs)—putative precursor lesions to PDAC—revealed that individual patients can harbour multiple *KRAS* hotspot mutations in spatially distinct PanINs and that more than one

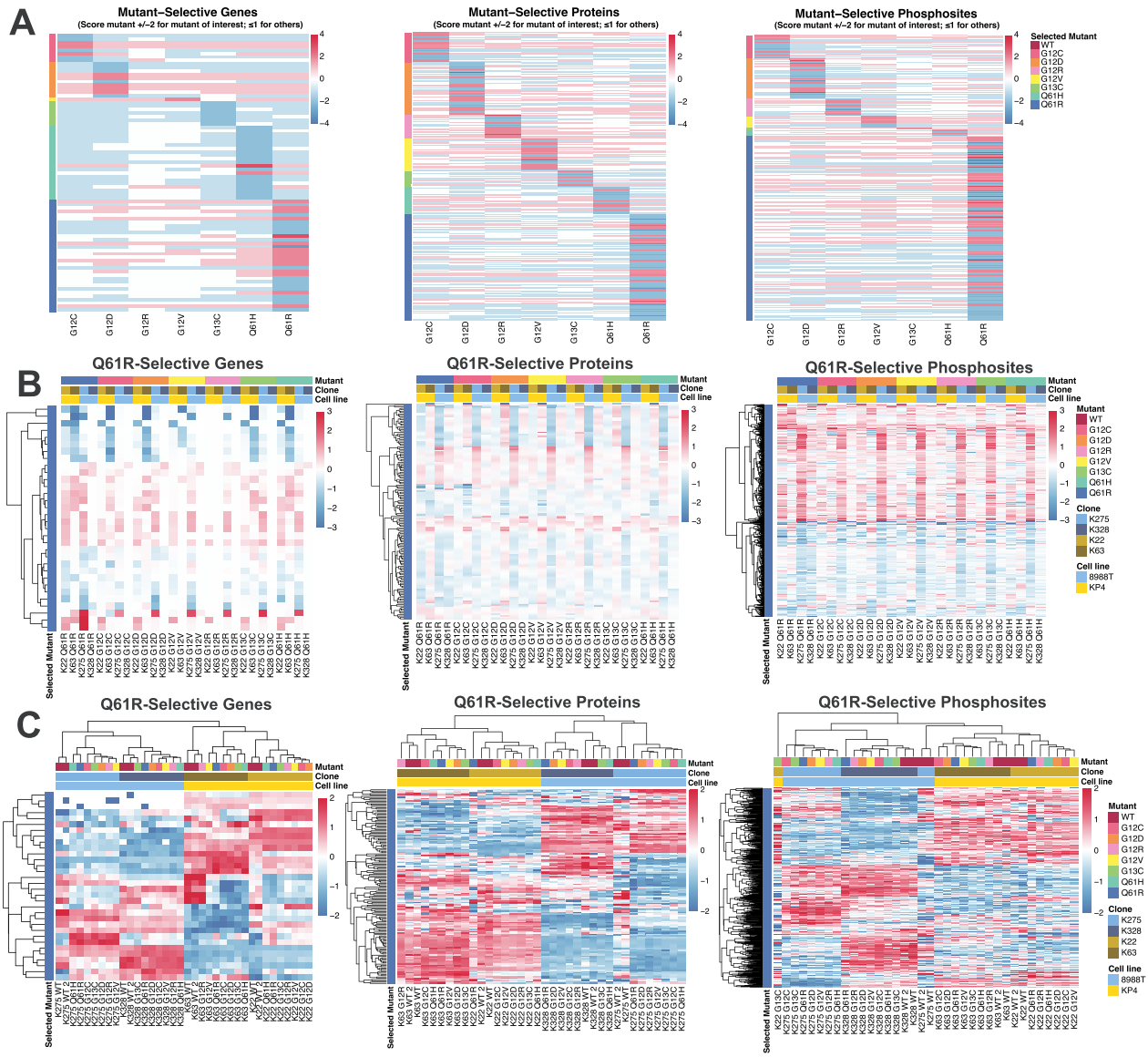


Figure 6 Identification of mutant-selective signatures across multi-omic layers. (A) Heatmaps of transcriptomic, proteomic, and phosphoproteomic features (genes, proteins, and phosphosites) meeting mutant-selective criteria (upregulated in ≥2 clones or downregulated in ≤−2 clones) for a given KRAS mutant and differentially expressed in ≤1 clone for other mutants (relative to WT) reveal limited allele specificity. Colour scale is number of upregulated (+) or downregulated (−) clones (out of four) for that feature (rows) of a given variant (columns). (B) Relative abundance (colour scale denotes $\log_2$ fold-change relative to $KRAS^{WT}$) for $KRAS^{Q61R}$-selective candidates [in (A); rows] across all clones and mutant variants (columns) shows similarity in direction of expression across all layers. (C) Supervised hierarchical clustering analyses of $KRAS^{Q61R}$-selective genes (transcriptome), proteins (proteome), and phosphosites (phosphoproteome) in (A). Colour scale denotes row-normalized expression.

KRAS mutation can be detected within the same PanIN, indicating that different alleles can arise in parallel during early tumour development [43]. Furthermore, the frequency of some mutations (e.g. Q61) may be overrepresented in PanINs compared to PDAC [43, 44]. These findings imply that extrinsic selective pressures such as cellular state, tissue context, and micro-environmental cues may amplify or constrain the subtle intrinsic biochemical differences between KRAS mutants throughout tumour evolution. Similarly, the emergence of a wide variety of secondary *KRAS* mutations in patients treated with KRAS inhibitors [45–48] suggests that diverse alleles can substitute for one another to mediate resistance. These data suggest that the presence of mutant KRAS itself, rather than a specific allele, is sufficient to sustain oncogenic signalling of advanced cancer cells under therapeutic selection. Together, these observations would argue that KRAS allele identity exerts a relatively minor influence on tumour cell behaviour compared to the broader cellular and evolutionary context in which it operates. This implies that allele-specific phenotypes arise not from intrinsic KRAS differences alone, but from the interplay of these differences with selective pressures present in the tumour microenvironment that define cellular states, though formal proof requires further experimental validation *in vivo*. Ultimately, our work sets the stage for investigating how cellular state and microenvironmental cues intersect with KRAS allele identity to shape tumour biology and therapeutic response.

Conclusions

By combining genotype-matched transcriptomic, proteomic, and phosphoproteomic data in reconstituted isogenic PDAC cells differing solely in KRAS mutant variant expression, we found that cellular context exerts a stronger influence on molecular outputs than *KRAS* allele identity, challenging the prevailing view that individual variants may drive distinct signalling programmes. As a consequence, oncogenic KRAS orchestrates a relatively narrow molecular programme shared across common mutant variants and previously reported KRAS-dependent transcriptomic and phosphoproteomic datasets. Pathway-level analyses of our multi-omic molecular profiles revealed shared signalling features across mutants, including suppression of interferon response genes and enrichment of ERK1/2 substrate phosphosites with reciprocal attenuation of DYRK kinase substrates. Together, these data provide a robust molecular omics resource of KRAS mutant signalling across variants in cancer.

Supplementary material

Supplementary material is available at *Molecular Omics* online.

Acknowledgements

We thank the Muzumdar and Liu lab members for helpful discussions and invaluable feedback; X. Ge, J. Singh., S. S. Agabiti, and W. Li for technical support; C. F. Ruiz for assistance with RNA-seq analysis; the Yale Center for Genome Analysis for library preparation, RNA-sequencing, and whole exome sequencing; the W. M. Keck DNA Sequencing Facility at Yale and Massachusetts General Hospital CCIB DNA Core for DNA sequencing; F. Fenteany and the Yale West Campus Flow Cytometry Facility for flow cytometry assistance; N. Joshi, the National Cancer Institute RAS Initiative, DSMZ, and RIKEN for cell lines; and T. Jacks, F. Zhang, and the NCI RAS Initiative for plasmid constructs.

Author contributions

Yanixa Quiñones-Avilés (Conceptualization [equal], Data curation [lead], Formal analysis [lead], Investigation [lead], Methodology [lead], Visualization [lead], Writing—original draft [lead]), Barbora Salovska (Formal analysis [lead], Investigation [lead], Methodology [lead], Software [lead], Visualization [lead], Writing—review & editing [equal]), Cassie S. Markham (Data curation [supporting], Formal analysis [supporting], Investigation [supporting], Methodology [supporting], Writing—review & editing [supporting]), Yi Di (Data curation [supporting], Formal analysis [supporting], Investigation [supporting], Methodology [supporting], Writing—review & editing [supporting]), Benjamin E. Turk (Formal analysis [supporting], Methodology [supporting], Software [supporting], Writing—review & editing [supporting]), Yansheng Liu (Formal analysis [supporting], Funding acquisition [lead], Investigation [supporting], Methodology [supporting], Project administration [lead], Resources [lead], Supervision [lead], Writing—review & editing [supporting]), and Mandar Deepak Muzumdar (Conceptualization [lead], Data curation [supporting], Formal analysis [supporting], Funding acquisition [lead], Methodology [supporting], Project administration [lead], Resources [supporting], Supervision [lead], Writing—original draft [lead])

Conflicts of interest

M.D.M. is an inventor on a patent applied for by Yale University that is unrelated to this work. M.D.M. received research funding from a Genentech supported American Association for Cancer Research (AACR) grant and an honorarium from Nested Therapeutics. All other authors declare no competing interests.

Funding

Y.Q.-A. was supported by a National Cancer Institute Ruth L. Kirschstein National Research Service Award Individual Predoctoral Fellowship (F31-CA265173) and a predoctoral fellowship from the Yale Cancer Biology Training Grant (T32-CA193200). C.S.M. was supported by a National Science Foundation Graduate Research Fellowship. Y.L. acknowledges support from a Yale Cancer Center Internal Pilot Grant supported by the Swebilius Trust and from the National Institute of General Medical Sciences (NIGMS, R35-GM158073). M.D.M. acknowledges support from an NIH Director's New Innovator Award (DP2-CA248136), NCI Mentored Clinical Scientist Research Career Development Award (K08-CA2080016), American Cancer Society Institutional Research Grant (IRG 17-172-57), Lustgarten Foundation Therapeutics-Focused Research Program, NCI R01-CA276108, and in part, the Yale Comprehensive Cancer Center Support Grant (P30-CA016359). The content is solely the responsibility of the authors and does not necessarily represent the official views of the National Institutes of Health.

Data availability

The mass spectrometry data and raw output tables have been deposited in the ProteomeXchange Consortium via the PRIDE [49] partner repository with the dataset identifier PXD071086. RNA-sequencing data have been deposited in NCBI Gene Expression Omnibus (GEO) and are accessible through GEO Series accession number GSE314073. Exome sequencing data have been deposited in Sequence Read Archive under accession number PRJNA1442763. Plasmids generated in this study will be deposited in Addgene. All other unique/stable reagents generated in this study are available with a completed materials transfer agreement.

References

1. Rahib L, Smith BD, Aizenberg R *et al.* Projecting cancer incidence and deaths to 2030: the unexpected burden of thyroid, liver, and pancreas cancers in the United States. *Cancer Res* 2014;**74**:2913–21. https://doi.org/10.1158/0008-5472.CAN-14-0155
2. Varghese AM, Perry MA, Chou JF *et al.* Clinicogenomic landscape of pancreatic adenocarcinoma identifies KRAS mutant dosage as prognostic of overall survival. *Nat Med* 2025;**31**:466–77. https://doi.org/10.1038/s41591-024-03362-3
3. Waters AM, Der CJ. KRAS: the critical driver and therapeutic target for pancreatic cancer. *Cold Spring Harb Perspect Med* 2018;**8**:a031435. https://doi.org/10.1101/cshperspect.a031435
4. Hunter JC, Manandhar A, Carrasco MA *et al.* Biochemical and structural analysis of common cancer-associated KRAS mutations. *Mol Cancer Res* 2015;**13**:1325–35. https://doi.org/10.1158/1541-7786.mcr-15-0203
5. Gebregiworgis T, Kano Y, St-Germain J *et al.* The Q61H mutation decouples KRAS from upstream regulation and renders cancer cells

resistant to SHP2 inhibitors. *Nat Commun* 2021;**12**:6274. https://doi.org/10.1038/s41467-021-26526-y
6. Hammond DE, Mageean CJ, Rusilowicz EV *et al.* Differential reprogramming of isogenic colorectal cancer cells by distinct activating KRAS mutations. *J Proteome Res* 2015;**14**:1535–46. https://doi.org/10.1021/pr501191a
7. Tahir R, Renuse S, Udainiya S *et al.* Mutation-specific and common phosphotyrosine signatures of KRAS G12D and G13D alleles. *J Proteome Res* 2021;**20**:670–83. https://doi.org/10.1021/acs.jproteome.0c00587
8. Hobbs GA, Baker NM, Miermont AM *et al.* Atypical KRAS(G12R) mutant is impaired in PI3K signaling and macropinocytosis in pancreatic cancer. *Cancer Discov* 2020;**10**:104–23. https://doi.org/10.1158/2159-8290.CD-19-1006
9. Stolze B, Reinhart S, Bulllinger L *et al.* Comparative analysis of KRAS codon 12, 13, 18, 61, and 117 mutations using human MCF10A isogenic cell lines. *Sci Rep* 2015;**5**:8535. https://doi.org/10.1038/srep08535
10. Klomp JA, Klomp JE, Stalnecker CA *et al.* Defining the KRAS- and ERK-dependent transcriptome in KRAS-mutant cancers. *Science.* 2024;**384**:eadk0775. https://doi.org/10.1126/science.adk0775
11. Klomp JE, Diehl JN, Klomp JA *et al.* Determining the ERK-regulated phosphoproteome driving KRAS-mutant cancer. *Science* 2024;**384**:eadk0850. https://doi.org/10.1126/science.adk0850
12. Kabella N, Bayer FP, Stamatiou K *et al.* Proteomic analyses identify targets, pathways, and cellular consequences of oncogenic KRAS signaling. *Sci Signal* 2025;**18**:eadt6552. https://doi.org/10.1126/scisignal.adt6552
13. Muzumdar MD, Chen P-Y, Dorans KJ *et al.* Survival of pancreatic cancer cells lacking KRAS function. *Nat Commun* 2017:10-23 2017;**8**:1–19. https://doi.org/doi:10.1038/s41467-017-00942-5
14. Akama-Garren EH, Joshi NS, Tammela T *et al.* A modular assembly platform for rapid generation of DNA constructs. *Sci Rep* 2016;**6**:16836. https://doi.org/10.1038/srep16836
15. Liu Y, Mi Y, Mueller T *et al.* Multi-omic measurements of heterogeneity in HeLa cells across laboratories. *Nat Biotechnol* 2019;**37**:314–22. https://doi.org/10.1038/s41587-019-0037-y
16. Gao Q, Zhu H, Dong L *et al.* Integrated proteogenomic characterization of HBV-related hepatocellular carcinoma. *Cell* 2019/10/03/ 2019;**179**:561–577.e22. https://doi.org/10.1016/j.cell.2019.08.052
17. Mehnert M, Li W, Wu C *et al.* Combining rapid data independent acquisition and CRISPR gene deletion for studying potential protein functions: a case of HMGN1. *Proteomics.* 2019;**19**:e1800438. https://doi.org/10.1002/pmic.201800438
18. Bruderer R, Muntel J, Muller S *et al.* Analysis of 1508 plasma samples by capillary-flow data-independent acquisition profiles proteomics of weight loss and maintenance. *Mol Cell Proteomics* 2019;**18**:1242–54. https://doi.org/10.1074/mcp.RA118.001288
19. Bruderer R, Bernhardt OM, Gandhi T *et al.* Optimization of experimental parameters in data-independent mass spectrometry significantly increases depth and reproducibility of results. *Mol Cell Proteomics* 2017;**16**:2296–309. https://doi.org/10.1074/mcp.RA117.000314
20. Love MI, Huber W, Anders S. Moderated estimation of fold change and dispersion for RNA-seq data with DESeq2. *Genome Biol* 2014;**15**:550. https://doi.org/10.1186/s13059-014-0550-8
21. Gao E, Li W, Wu C *et al.* Data-independent acquisition-based proteome and phosphoproteome profiling across six melanoma cell lines reveals determinants of proteotypes. *Mol Omics* 2021;**17**:413–25. https://doi.org/10.1039/d0mo00188k
22. Bekker-Jensen DB, Bernhardt OM, Hogrebe A *et al.* Rapid and site-specific deep phosphoproteome profiling by data-independent acquisition without the need for spectral libraries. *Nat Commun* 2020;**11**:787. https://doi.org/10.1038/s41467-020-14609-1
23. Rosenberger G, Liu Y, Rost HL *et al.* Inference and quantification of peptidoforms in large sample cohorts by SWATH-MS. *Nat Biotechnol* 2017;**35**:781–8. https://doi.org/10.1038/nbt.3908
24. Smyth GK. Limma: Linear models for microarray data. In: Gentleman R, Carey VJ, Huber W *et al.* (eds.), *Bioinformatics and Computational Biology Solutions Using R and Bioconductor*, pp. 397–420. Springer: New York, 2005.
25. Olsen JV, Blagoev B, Gnad F *et al.* Global, in vivo, and site-specific phosphorylation dynamics in signaling networks. *Cell* 2006;**127**:635–48. https://doi.org/10.1016/j.cell.2006.09.026
26. Voss H, Schlumbohm S, Barwikowski P *et al.* HarmonizR enables data harmonization across independent proteomic datasets with appropriate handling of missing values. *Nat Commun* 2022;**13**:3523. https://doi.org/10.1038/s41467-022-31007-x
27. Wang S, Di Y, Yang Y *et al.* PTMoreR-enabled cross-species PTM mapping and comparative phosphoproteomics across mammals. *Cell Rep Methods* 2024;**4**:100859. https://doi.org/10.1016/j.crmeth.2024.100859
28. Ritchie ME, Phipson B, Wu D *et al.* Limma powers differential expression analyses for RNA-sequencing and microarray studies. *Nucleic Acids Res* 2015;**43**:e47, 10.1093/nar/gkv007.
29. Zhou Y, Zhou B, Pache L *et al.* Metascape provides a biologist-oriented resource for the analysis of systems-level datasets. *Nat Commun* 2019/04/03 2019;**10**:1523. https://doi.org/10.1038/s41467-019-09234-6
30. Liberzon A, Birger C, Thorvaldsdottir H *et al.* The molecular signatures database (MSigDB) hallmark gene set collection. *Cell Syst* 2015;**1**:417–25. https://doi.org/10.1016/j.cels.2015.12.004
31. Liu Y, Beyer A, Aebersold R. On the dependency of cellular protein levels on mRNA abundance. *Cell.* 2016;**165**:535–50. https://doi.org/10.1016/j.cell.2016.03.014
32. Johnson JL, Yaron TM, Huntsman EM *et al.* An atlas of substrate specificities for the human serine/threonine kinome. *Nature.* 2023;**613**:759–66. https://doi.org/10.1038/s41586-022-05575-3
33. Pratilas CA, Taylor BS, Ye Q *et al.* ^{V600}EBRAF is associated with disabled feedback inhibition of RAF−MEK signaling and elevated transcriptional output of the pathway. *Proc Natl Acad Sci* 2009;**106**:4519–24. https://doi.org/doi:10.1073/pnas.0900780106
34. Vogel C, Marcotte EM. Insights into the regulation of protein abundance from proteomic and transcriptomic analyses. *Nat Rev Genet* 2012;**13**:227–32. https://doi.org/10.1038/nrg3185
35. Ebia MI, Blais EM, Cui Y *et al.* Evaluating the effect of KRAS variants on survival outcomes and therapy response in pancreatic cancer. *JCO Precis Oncol* 2025;**9**:e2400684. https://doi.org/10.1200/PO-24-00684
36. McIntyre CA, Grimont A, Park J *et al.* Distinct clinical outcomes and biological features of specific KRAS mutants in human pancreatic cancer. *Cancer Cell* 2024;**42**:1614–1629 e5. https://doi.org/10.1016/j.ccell.2024.08.002
37. Li S, Balmain A, Counter CM. A model for RAS mutation patterns in cancers: finding the sweet spot. *Nat Rev Cancer* 2018;**18**:767–77. https://doi.org/10.1038/s41568-018-0076-6
38. Cook JH, Melloni GEM, Gulhan DC *et al.* The origins and genetic interactions of KRAS mutations are allele- and tissue-specific. *Nat Commun* 2021;**12**:1–14. https://doi.org/doi:10.1038/s41467-021-22125-z

39. Zafra MP, Parsons MJ, Kim J *et al.* An in vivo KRAS allelic series reveals distinct phenotypes of common oncogenic variants. *Cancer Discov* 2020;**10**:1654–71. https://doi.org/10.1158/2159-8290.CD-20-0442
40. Huang HC, Deng Q, Guo L *et al.* Kras G12C- and G12D-driven lung cancers differ in oncogenic potency, immunogenicity, and relapse after Kras inhibition in mouse models. *Sci Transl Med* 2026;**18**:eadq6647. https://doi.org/10.1126/scitranslmed.adq6647
41. Park JT, Johnson N, Liu S *et al.* Differential in vivo tumorigenicity of diverse KRAS mutations in vertebrate pancreas: a comprehensive survey. *Oncogene.* 2015;**34**:2801–6. https://doi.org/10.1038/onc.2014.223
42. Muthalagu N, Monteverde T, Raffo-Iraolagoitia X *et al.* Repression of the type I interferon pathway underlies MYC- and KRAS-dependent evasion of NK and B cells in pancreatic ductal adenocarcinoma. *Cancer Discov* 2020;**10**:872–87. https://doi.org/10.1158/2159-8290.CD-19-0620
43. Braxton AM, Kiemen AL, Grahn MP *et al.* 3D genomic mapping reveals multifocality of human pancreatic precancers. *Nature.* 2024;**629**:679–87. https://doi.org/10.1038/s41586-024-07359-3
44. TCGA Research Network. Integrated genomic characterization of pancreatic ductal adenocarcinoma. *Cancer Cell* 2017;**32**:185–203.e13. https://doi.org/10.1016/j.ccell.2017.07.007
45. Dilly J, Hoffman MT, Abbassi L *et al.* Mechanisms of resistance to oncogenic KRAS inhibition in pancreatic cancer. *Cancer Discov* 2024;**14**:2135–61. https://doi.org/10.1158/2159-8290.CD-24-0177
46. Awad MM, Liu S, Rybkin II *et al.* Acquired resistance to KRAS(G12C) inhibition in cancer. *N Engl J Med* 2021;**384**:2382–93. https://doi.org/10.1056/NEJMoa2105281
47. Sacher A, LoRusso P, Patel MR *et al.* Single-agent divarasib (GDC-6036) in solid tumors with a KRAS G12C mutation. *N Engl J Med* 2023;**389**:710–21. https://doi.org/10.1056/NEJMoa2303810
48. Zhao Y, Murciano-Goroff YR, Xue JY *et al.* Diverse alterations associated with resistance to KRAS(G12C) inhibition. *Nature.* 2021;**599**:679–83. https://doi.org/10.1038/s41586-021-04065-2
49. Perez-Riverol Y, Bandla C, Kundu DJ *et al.* The PRIDE database at 20 years: 2025 update. *Nucleic Acids Res* 2025;**53**:D543–d553. https://doi.org/10.1093/nar/gkae1011

© The Author(s) 2026. Published by Oxford University Press. This is an Open Access article distributed under the terms of the Creative Commons Attribution-NonCommercial License (https://creativecommons.org/licenses/by-nc/4.0/), which permits non-commercial re-use, distribution, and reproduction in any medium, provided the original work is properly cited. For commercial re-use, please contact reprints@oup.com for reprints and translation rights for reprints. All other permissions can be obtained through our RightsLink service via the Permissions link on the article page on our site—for further information please contact journals.permissions@oup.com.
Molecular Omics, 2026, **22**, 1–17
https://doi.org/10.1093/molecular-omics/aaiag022
Research Article